

Kdm2a inhibition in skeletal muscle improves metabolic flexibility in obesity

Received: 17 July 2024

Accepted: 17 December 2024

Published online: 27 January 2025

 Check for updates

Yuhan Wang^{1,9}, Hao Xie^{1,2,9}, Qianrui Liu^{1,9}, Na Wang^{1,9}, Xi Luo¹, Fei Sun¹, Jinghan Zhu³, Ruihan Dong¹, Yi Wang¹, Jia Gao¹, Zhichao Gao¹, Teng Huang¹, Xin Liu⁴, Qilin Yu¹, Ting Wang¹, Yang Li¹, Danni Song¹, Shiwei Liu⁵, Shu Zhang¹, Hao Yin⁶, Wen Kong⁷ & Cong-Yi Wang^{5,8}

Skeletal muscle is a critical organ in maintaining homeostasis against metabolic stress, and histone post-translational modifications are pivotal in those processes. However, the intricate nature of histone methylation in skeletal muscle and its impact on metabolic homeostasis have yet to be elucidated. Here, we report that mitochondria-rich slow-twitch myofibers are characterized by significantly higher levels of H3K36me2 along with repressed expression of *Kdm2a*, an enzyme that specifically catalyses H3K36me2 demethylation. Deletion or inhibition of *Kdm2a* shifts fuel use from glucose under cold challenge to lipids under obese conditions by increasing the proportion of mitochondria-rich slow-twitch myofibers. This protects mice against cold insults and high-fat-diet-induced obesity and insulin resistance. Mechanistically, *Kdm2a* deficiency leads to a marked increase in H3K36me2 levels, which then promotes the recruitment of Mrg15 to the *Esrrg* locus to process its precursor messenger RNA splicing, thereby reshaping skeletal muscle metabolic profiles to induce slow-twitch myofiber transition. Collectively, our data support the role of *Kdm2a* as a viable target against metabolic stress.

Skeletal muscle constitutes 40–50% of total body mass and accounts for approximately 30% of basal energy expenditure¹. In general, skeletal muscle is characterized by flexibility of changes in terms of muscle mass, metabolic characteristics and myofiber type, thereby maintaining the homeostasis of metabolism^{2,3}, and increasing attention is being directed towards targeting skeletal muscle to optimize systemic metabolism^{3–8}. Indeed, there is convincing evidence that obesity is generally manifested by a lower proportion of slow-twitch myofibers

(STMs) along with mitochondrial dysfunction, which then predisposes to the development of insulin resistance and other severe metabolic disorders, such as type 2 diabetes, fatty liver and cardiovascular disease^{9–17}.

Previous studies, including our own, have demonstrated that epigenetic mechanisms serve as a bridge to link environmental insults to the pathogenesis of metabolic disorders in genetically predisposed subjects^{18–23}. Specifically, post-translational modifications (PTMs) of histone proteins are considered to be an important epigenetic factor

¹Department of Respiratory and Critical Care Medicine, The Center for Biomedical Research, NHC Key Laboratory of Respiratory Diseases, Tongji Hospital, Tongji Medical College, Huazhong University of Science and Technology, Wuhan, China. ²Department of Clinical Laboratory, Institute of Translational Medicine, Renmin Hospital of Wuhan University, Wuhan, China. ³Department of Hepatic Surgery, Tongji Hospital, Tongji Medical College, Huazhong University of Science and Technology, Wuhan, China. ⁴Department of Interventional Radiology, Renmin Hospital of Wuhan University, Wuhan, China.

⁵Tongji Shanxi Hospital, Shanxi Bethune Hospital, Shanxi Academy of Medical Science, Third Hospital of Shanxi Medical University, the Key Laboratory of Endocrine and Metabolic Diseases of Shanxi Province, Taiyuan, China. ⁶Organ Transplant Center, Shanghai Changzheng Hospital (Second Affiliated Hospital of Naval Medical University), Shanghai, China. ⁷Department of Endocrinology, Union Hospital, Tongji Medical College, Huazhong University of Science and Technology, Wuhan, China. ⁸The Center for Biomedical Research, Tongji Hospital Research Building, Tongji Hospital, Tongji Medical College, Huazhong University of Science and Technology, Wuhan, China. ⁹These authors contributed equally: Yuhan Wang, Hao Xie, Qianrui Liu, Na Wang.

✉ e-mail: szhang@tjh.tjmu.edu.cn; yinhaoshanghai@163.com; wenly-kong@163.com; wangcy@tjh.tjmu.edu.cn

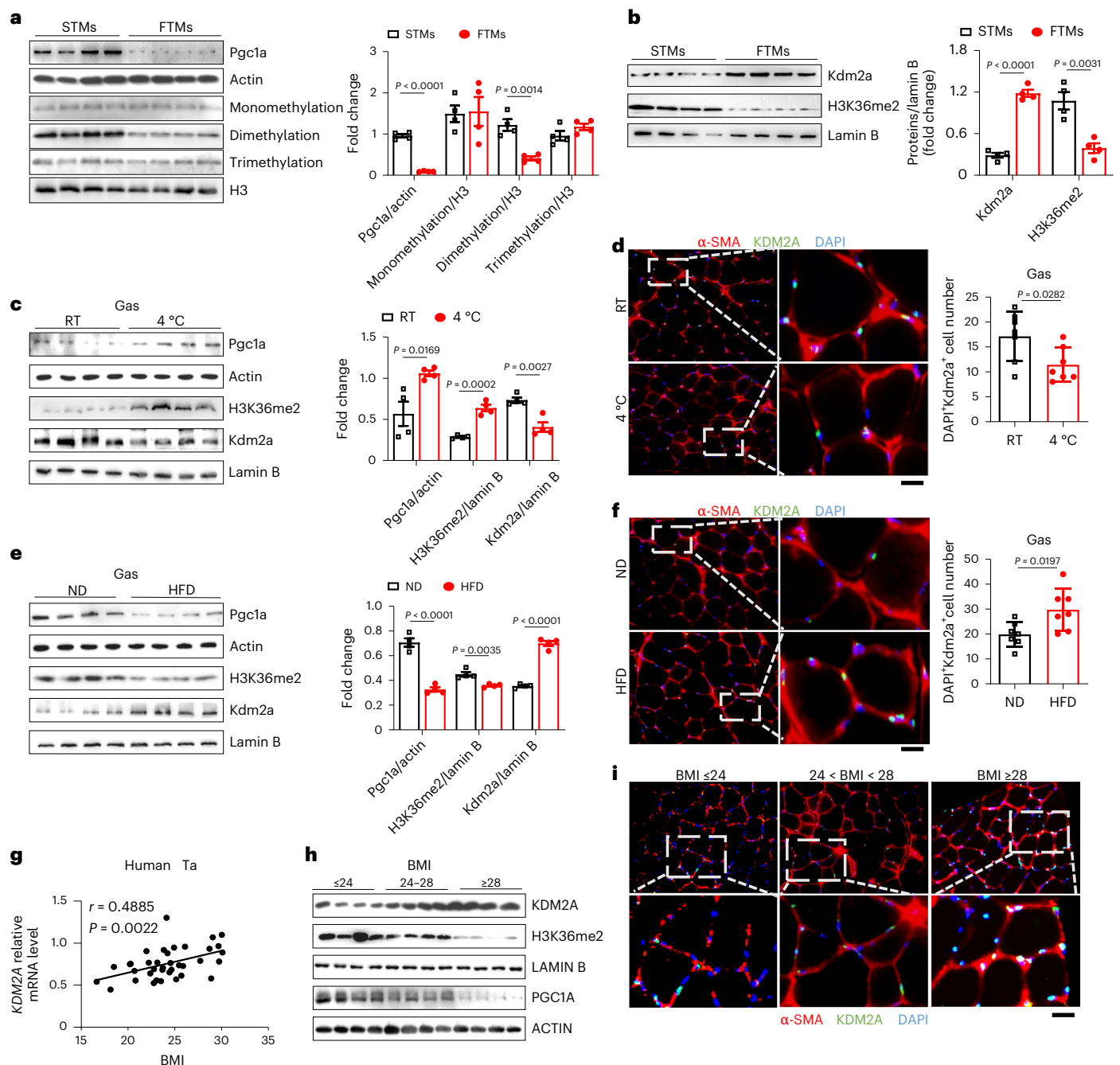


Fig. 1 | Kdm2a catalyzes H3K36me2 demethylation and reduces STM

proportion. **a**, Western blot analysis of Pgc1a, monomethylation, dimethylation and trimethylation levels between STMs (soleus) and FTMs (extensor digitorum longus) from male WT mice fed with a normal diet ($n = 4$); protein quantitative analysis is shown on the right. **b**, Western blot analysis of Kdm2a and H3K36me2 between STMs and FTMs from male WT mice fed with a normal diet ($n = 4$); protein quantitative analysis is shown on the right. **c**, Western blot analysis of Pgc1a, H3K36me2 and Kdm2a from Gas tissues of male WT mice from room temperature (RT) and cold-adapted (4 °C) groups ($n = 4$ per group); protein quantitative analysis is shown on the right. **d**, Representative immunostaining of Kdm2a (green), α -SMA (red) and DAPI (blue) in cross sections of Gas tissues from male WT mice from RT and cold-adapted (4 °C) groups. Scale bars, 50 μm . DAPI⁺Kdm2a⁺ cell number was counted (right) ($n = 7$ per group). **e**, Western blot analysis of Pgc1a, Kdm2a and H3K36me2 from Gas tissues of male mice

fed a normal diet (ND) and HFD ($n = 4$ per group); protein quantitative analysis is shown on the right. **f**, Representative immunostaining of Kdm2a, α -SMA (red) and DAPI (blue) in cross sections of Gas tissues from ND-fed and HFD-fed male mice. Scale bars, 50 μm . DAPI⁺Kdm2a⁺ cell number was counted (right) ($n = 7$ per group). **g**, Correlation analysis between BMI and KDM2A levels in human tibialis anterior (Ta) samples ($n = 37$). **h**, Western blot showing KDM2A, H3K36me2 and PGC1A expression in Ta tissues of lean subjects (BMI ≤ 24 , $n = 3$), overweight subjects ($24 < \text{BMI} < 28$, $n = 3$) and obese subjects (BMI ≥ 28 , $n = 3$). **i**, Representative immunostaining of KDM2A, α -SMA (red) and DAPI (blue) in Ta tissue cross sections from lean subjects (BMI ≤ 24 , $n = 7$), overweight subjects ($24 < \text{BMI} < 28$, $n = 7$) and obese subjects (BMI ≥ 28 , $n = 7$). Scale bars, 50 μm . Data are represented as mean \pm s.e.m. Statistical significance was assessed by unpaired two-sided Student's *t*-test (**a–f**) and two-sided Spearman's correlation (**g**).

in regulating the function of skeletal muscle, with rapid responses and a variety of modification characteristics¹⁸. Histone acetylation has been demonstrated to have a critical role in the regulation of GLUT4 expression, glucose uptake and insulin-mediated glycogen synthesis²⁴. However, the intricate nature of histone methylation in skeletal muscle and its impact on metabolic homeostasis have yet to be elucidated.

In the current study, we identified a significant discrepancy in terms of histone H3 dimethylation at lysine (K) 36 (H3K36me2) between STMs and fast-twitch myofibers (FTMs) in both male and female mice. In general, the mitochondria-rich STMs, represented by the soleus, are prone to aerobic metabolism, which uses both glucose and lipids as the main fuel. By contrast, the BAF60c-driven FTMs³, represented by the extensor digitorum longus, are prone to anaerobic metabolism by using glucose as the major energy source. In the majority of experiments, male mice have been used as the representative. We found that lysine (K)-specific demethylase 2A (Kdm2a; <https://www.ncbi.nlm.nih.gov/gene/225876>), a histone demethylase, regulates the FTM–STM transition. Therefore, deletion or inhibition of *Kdm2a* promptly shifts the fuel use from glucose under cold challenge to lipid in the obese condition by increasing the proportion of mitochondria-rich STMs, which then enhances the capability of mice against cold insult and protects the mice from high-fat-diet (HFD)-induced obesity and insulin resistance. Mechanistically, Kdm2a promotes histone 3 (H3) demethylation at the *Esrrg* locus and prevents Mrg15 from splicing *Esrrg* precursor messenger RNA (pre-mRNA), which inhibits lipid oxidation and the STM transition in skeletal muscle. These findings not only fill a gap in our understanding of the mechanisms underlying skeletal muscle myofiber transition but also suggest that Kdm2a could be a promising target against metabolic stress in clinical settings.

Results

Kdm2a catalyses H3K36me2 demethylation and reduces STM proportion

We fortuitously observed significantly elevated levels of histone lysine-pan-dimethylation in both male and female aerobic STMs along with markedly higher expression of proliferator-activated receptor gamma coactivator 1- α (Pgc1 α) (Fig. 1a and Supplementary Fig. 1a), a key regulator of energy metabolism and mitochondrial biogenesis^{25–28}, compared to the anaerobic FTMs. By contrast, no discernible difference in terms of histone lysine-pan-monomethylation and trimethylation was noted (Fig. 1a and Supplementary Fig. 1a). These results prompted us to focus on the enzymes relevant to lysine-pan-dimethylation in both STMs and FTMs. Interestingly, lysine-specific demethylase 2A (Kdm2a), which is known to specifically catalyse the demethylation of H3K36me2, was noted to be selectively highly expressed in FTMs compared to the other lysine-pan-dimethylation enzymes at both mRNA (Extended Data Fig. 1a) and protein levels (Fig. 1b and Supplementary Fig. 1b), which was coupled with a significant decrease in H3K36me2 levels (Fig. 1b and Supplementary Fig. 1b). These findings support a critical role of Kdm2a in the regulation of H3K36me2 levels in skeletal muscle, regardless of gender difference.

To further address the above question, we exposed male mice to cold temperatures, as cold adaptation is a powerful inducer of non-shivering thermogenesis and enhances the metabolic capacity of skeletal muscle by increasing the proportion of STMs^{29–33}. Following 2 weeks of cold adaptation, enhanced Pgc1 α expression was detected in the gastrocnemius (Gas), a type of skeletal muscle that contains both STMs and FTMs, with manifestations of a high degree of flexibility in response to different stimuli coupled with a marked increase of H3K36me2 levels and a significant decrease in Kdm2a expression (Fig. 1c and Supplementary Fig. 1c). Immunostaining of Gas sections further validated a conspicuous reduction of Kdm2a expression in myofibers following a sustained cold insult (Fig. 1d). Of note, a similar phenotype was also observed in cold-stimulated C2C12 myotubes (Extended Data Fig. 1b). Unlike cold-induced non-shivering

thermogenesis, obesity induced by excessive accumulation of glucose and lipids is commonly associated with decreased STMs along with a reduced capacity to withstand cold challenge^{15,16,34,35}. Therefore, we next challenged the mice to 16 weeks of HFD induction. Indeed, HFD induced a significant reduction of Pgc1 α expression, accompanied by decreased H3K36me2 levels and increased Kdm2a expressions in skeletal muscle (Fig. 1e). The increased Kdm2a expression was also confirmed by immunostaining of Gas sections (Fig. 1f). Similarly, we detected increased Kdm2a and decreased H3K36me2 levels in a hyperglycaemia model (Extended Data Fig. 1c). Treatment of C2C12 myotubes with either palmitic acid (0.8 mM) (Extended Data Fig. 1d) or high glucose (30 mM) (Extended Data Fig. 1e) yielded analogous results. We also established female cold-adapted (Supplementary Fig. 1c), HFD-challenged (Supplementary Fig. 1d) and hyperglycemic mouse models (Supplementary Fig. 1e), and similar results were observed.

To validate the above findings in humans, we examined the relationship between body mass index (BMI) and KDM2A expression levels in the human tibialis anterior muscle. Remarkably, a positive correlation was detected between KDM2A expression and BMI (Fig. 1g). Specifically, a BMI-dependent upregulation of KDM2A expression was noted, which was coupled with decreased H3K36me2 levels and attenuated PGC1 α expression in the tibialis anterior muscle (Fig. 1h and Extended Data Fig. 1f). Immunostaining of tibialis anterior sections further confirmed the correlation between KDM2A expression in tibialis anterior myofibers and BMI (Fig. 1i and Extended Data Fig. 1g). Collectively, our data support that Kdm2a catalyses H3K36me2 demethylation, thus reducing the proportion of STM in the Gas upon the challenge of metabolic stress.

Enhanced glucose consumption in *Kdm2a* knockout mice under cold insult

To further address the functional impact of Kdm2a on the metabolic properties of skeletal muscle, an inducible skeletal muscle-specific *Kdm2a* knockout (KO) mouse model (referred as *Kdm2a*^{SKO}) was developed by crossing *Kdm2a*^{fl/fl} mice with the *ACTA1-rtTA-tetO-Cre* mice, and *Kdm2a* deficiency was induced in 8-week-old mice by tetracycline (Supplementary Fig. 2a). In consideration of mouse reproduction, subsequent experiments were conducted in male mice. The *Kdm2a*^{SKO} mice and their control littermates were then subjected to a cold challenge. It was noted that the *Kdm2a*^{SKO} mice showed greater temperature stability following 2 weeks of cold challenge (Fig. 2a) and exhibited a higher random body temperature after completion of the cold challenge (Fig. 2b). A similar phenotype was also observed under the resting state (Supplementary Fig. 2i). However, there was no difference in Ucp1 and mitochondrial-complex-related gene expression in both subcutaneous fat (Supplementary Fig. 2j) and brown fat (Supplementary Fig. 2k), further demonstrating that *Kdm2a* deficiency specifically promotes skeletal muscle thermogenesis. It is noteworthy that the *Kdm2a*^{SKO} mice manifested significantly greater weight loss following the cold challenge (Fig. 2c), along with lower fasting blood glucose levels (Fig. 2d), improved glucose tolerance (Fig. 2e) and increased insulin sensitivity (Fig. 2f). Metabolic parameters including daytime thermogenesis (Fig. 2g), oxygen consumption (Fig. 2h) and carbon dioxide emission (Fig. 2i) were higher in *Kdm2a*^{SKO} mice upon completion of the cold challenge, and no perceptible difference in terms of food and water intake was detected (Extended Data Fig. 2a). Moreover, the *Kdm2a*^{SKO} mice manifested a higher consumption of glucose as evidenced by the higher respiratory exchange ratios (RERs) both in day and night following the cold challenge (Fig. 2j). Together, these data support that *Kdm2a* deficiency allows the mice to leverage more glucose to enhance energy production upon a cold challenge.

In line with the above observations, the *Kdm2a*^{SKO} mice were characterized by dark-coloured Gas muscles compared to that of wild-type (WT) mice following the cold challenge (Fig. 2k) but without a discernible difference in terms of muscle mass (Extended Data Fig. 2b),

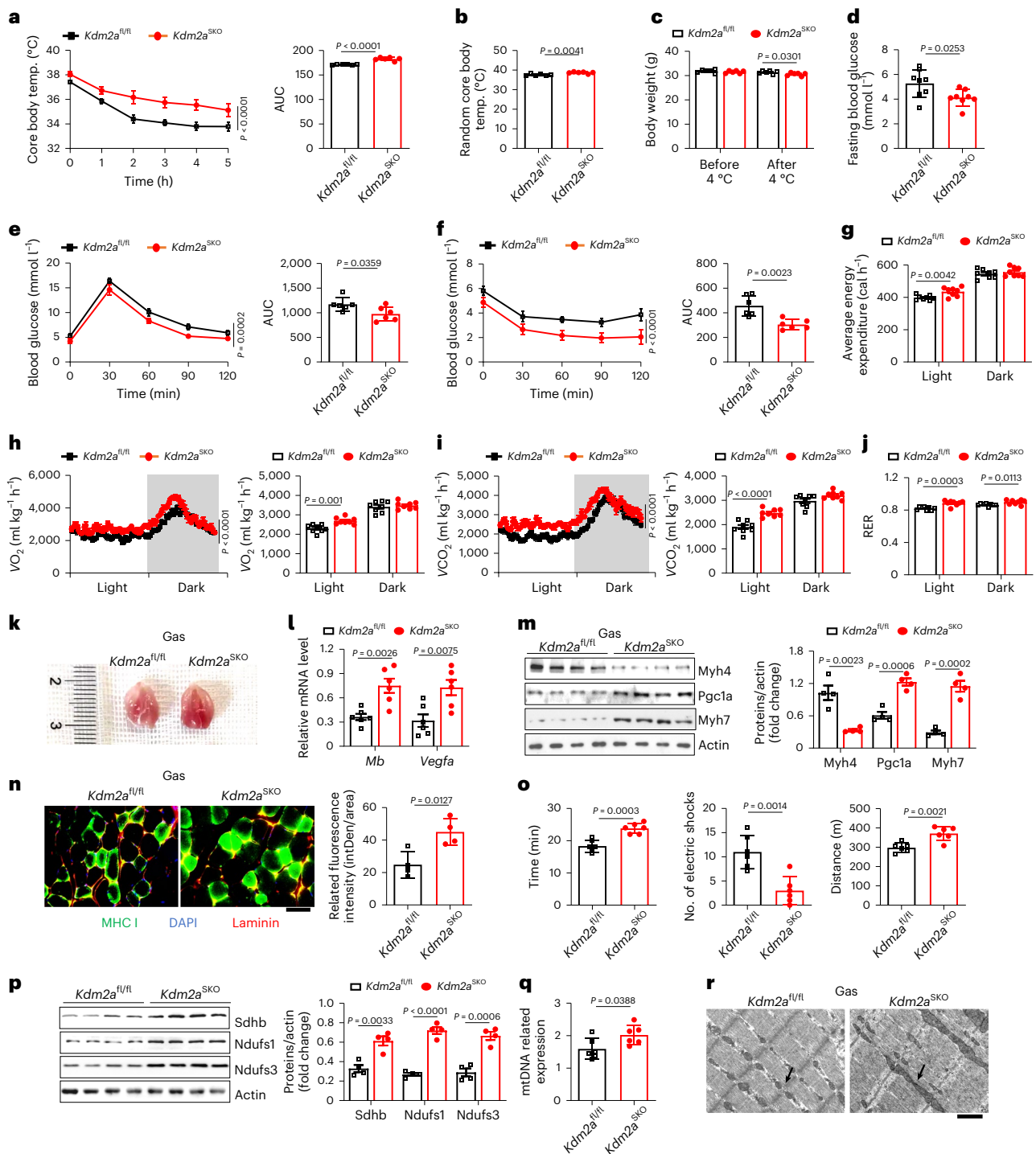


Fig. 2 | Enhanced glucose consumption in *Kdm2a*-KO mice under cold insult.

a, Core body temperature monitoring of *Kdm2a*^{fl/fl} and *Kdm2a*^{SKO} mice at 4 °C after cold adaptation ($n = 6$ per group). AUC, area under the curve. **b**, Random core body temperature of *Kdm2a*^{fl/fl} and *Kdm2a*^{SKO} mice ($n = 6$ per group). **c**, Body weight before and after cold adaptation of *Kdm2a*^{fl/fl} and *Kdm2a*^{SKO} mice ($n = 6$ per group). **d**, Fasting blood glucose of cold-adapted *Kdm2a*^{fl/fl} and *Kdm2a*^{SKO} mice ($n = 8$ per group). **e**, Intraperitoneal glucose tolerance test and **f**, insulin tolerance test of cold-adapted *Kdm2a*^{fl/fl} and *Kdm2a*^{SKO} mice ($n = 6$ per group). **g–j**, Parameters measured in metabolic cages during day and night conditions in *Kdm2a*^{fl/fl} and *Kdm2a*^{SKO} mice: average energy expenditure (**g**), oxygen consumption (VO_2) (**h**), Carbon dioxide emission (**i**) and RER (**j**) ($n = 8$ per group). **k**, Representative image of Gas tissue from *Kdm2a*^{fl/fl} and *Kdm2a*^{SKO} mice ($n = 6$ per group). **l**, RT–qPCR analysis of *Mb* and vascular endothelial growth factor (*Vegfa*) expression in Gas tissues from *Kdm2a*^{fl/fl} and *Kdm2a*^{SKO} mice ($n = 6$ per group). **m**, Western blot analysis of Myh4, Pgc1a and Myh7 in Gas tissues from

cold-adapted *Kdm2a*^{fl/fl} and *Kdm2a*^{SKO} mice ($n = 4$ per group). **n**, Representative immunofluorescence staining of Laminin (red), MHC I (green) and DAPI (blue) in frozen sections of Gas tissues from *Kdm2a*^{fl/fl} and *Kdm2a*^{SKO} mice. Scale bars, 50 μ m; $n = 4$ per group; intDen, integrated density. **o**, Endurance capacity test showing time to exhaustion (left), electric shock times (middle) and distance to exhaustion (right) of cold-adapted *Kdm2a*^{fl/fl} and *Kdm2a*^{SKO} mice ($n = 6$ per group). **p**, Western blot showing expression of mitochondrial biogenesis-related genes in *Kdm2a*^{fl/fl} and *Kdm2a*^{SKO} mice ($n = 4$ per group). **q**, Relative mitochondrial DNA (mtDNA) copy number analysis of cold-adapted *Kdm2a*^{fl/fl} and *Kdm2a*^{SKO} mice ($n = 6$ per group). **r**, Representative TEM micrographs of Gas tissues from *Kdm2a*^{fl/fl} and *Kdm2a*^{SKO} mice. Mitochondria are indicated by arrows. Scale bars, 10 μ m, $n = 4$ per group. Data are expressed as mean \pm s.e.m. Statistical significance was assessed by two-way ANOVA (**a**, **e**, **h**, **i**) followed by Bonferroni's multiple comparisons test or two-sided Student's *t*-test (**b–d**, **g**, **j**, **l–q**).

indicating an increased proportion of STMs featured by highly enriched mitochondria and myoglobin (*Mb*). Indeed, Gas muscles from *Kdm2a*^{SKO} mice exhibited augmented myoangiogenesis (Extended Data Fig. 2c,d) without a significant alteration in muscle area (Extended Data Fig. 2c) but significantly upregulated *Mb* and vascular endothelial growth factor expression (Fig. 2l). Western blot analysis further revealed increased *Pgc1a* and *Myh7* but decreased *Myh4* expressions (Fig. 2m). In particular, immunostaining of Gas sections confirmed a FTM-to-STM transition (Fig. 2n and Extended Data Fig. 2e), which was further confirmed by prolonged running endurance capacity (Fig. 2o and Supplementary Video 1). Of note, we also observed elevated expression of mitochondrial respiration-associated genes (*Ndufs1* and *Ndufs3* of complex I, *Sdhb* of complex II) (Fig. 2p) and increased mitochondrial DNA content (Fig. 2q) in the *Kdm2a*^{SKO} mice. Transmission electron microscopy (TEM) supported the above findings as evidenced by the increased mitochondrial numbers and cristae density in *Kdm2a*^{SKO} Gas muscles (Fig. 2r). It is noteworthy that no significant difference was found in terms of body weight (Extended Data Fig. 2f), glucose tolerance (Extended Data Fig. 2g) or insulin sensitivity (Extended Data Fig. 2h) between *Kdm2a*^{SKO} mice and their littermate controls under physiological condition; similar results were also observed for the expression of mitochondrial function-related genes and *Pgc1a* (Extended Data Fig. 2i,j).

To further confirm the above findings, *Kdm2a*-KO myoblasts were generated using the LentiCRISPR (v.2) approach. Western blotting verified that *Kdm2a* deficiency increased H3K36me2 levels (Extended Data Fig. 2k). Increased glucose uptake in *Kdm2a*-KO myotubes was detected upon 2 h of cold challenge (Extended Data Fig. 2l), which was consistent with the *in vivo* phenotype. Critically, we also observed enhanced myoangiogenesis (Extended Data Fig. 2m) and myofiber type transition (Extended Data Fig. 2m,n) along with improved mitochondrial function (Extended Data Fig. 2n,o) in the *Kdm2a*-KO myotubes upon 2 h of cold challenge. Taken together, our data support that loss of *Kdm2a* enhances glucose consumption to protect mice against cold insult by promoting mitochondria-rich STM transition.

Loss of *Kdm2a* promotes lipid consumption in HFD-induced mice

Given that obesity is generally coupled with mitochondrial dysfunction and reduction of the proportion of STMs^{17,36}, we next challenged *Kdm2a*^{SKO} male mice and littermate controls with a HFD for 16 weeks. Lower body weight was noted in *Kdm2a*^{SKO} mice after 12 weeks of HFD challenge (Fig. 3a), which became more significant following another 4 weeks of HFD induction (Fig. 3b). Notably, the *Kdm2a*^{SKO} mice also exhibited a decrease in fat mass, whereas lean mass remained relatively comparable (Fig. 3c). Moreover, *Kdm2a*^{SKO} mice displayed lower fasting blood glucose (Fig. 3d) and serum insulin levels (Fig. 3e) along with enhanced glucose tolerance (Fig. 3f and Extended Data Fig. 3a) and insulin sensitivity (Fig. 3g and Extended Data Fig. 3b). The mice were then subjected to metabolic analysis. The *Kdm2a*^{SKO} mice exhibited elevated rates of oxygen consumption (Fig. 3h), carbon dioxide emission (Fig. 3i) and energy expenditure (Fig. 3j) without a perceptible difference in terms of food and water intake (Extended Data Fig. 3c). In particular, the *Kdm2a*^{SKO} mice were characterized by enhanced β -oxidation as evidenced by lower RER values (Fig. 3k)^{26,37} coupled with elevated random core body temperature at room temperature (20–24 °C) following 16 weeks of HFD challenge (Fig. 3l). Together, these data support that *Kdm2a* deficiency allows mice to use more lipids for energy consumption upon a HFD challenge.

Upon completion of the HFD induction, the mice were immediately subjected to cold challenge as described in Supplementary Fig. 1f. Similarly, the *Kdm2a*^{SKO} mice exhibited an enhanced capacity to maintain their core body temperature upon the cold challenge under fasted conditions (Fig. 3m). The Gas muscles from *Kdm2a*^{SKO} mice were typically dark red (Fig. 3n), indicating highly enriched mitochondrion

and *Mb* content. No perceptible alterations were noted in terms of muscle mass (Extended Data Fig. 3d) or the average area of myotubes (Extended Data Fig. 3e). Western blot analysis (Fig. 3o), quantitative PCR with reverse transcription (RT-qPCR) (Extended Data Fig. 3g) and CD31 immunostaining (Extended Data Fig. 3f) confirmed that *Kdm2a* deficiency augmented myoangiogenesis as evidenced by the enhanced FTM-to-STM transition. The increased proportion of STMs was further validated by immunostaining of the tibialis anterior sections (Fig. 3p and Extended Data Fig. 3h,i) and by treadmill running assays, in which the HFD-induced *Kdm2a*^{SKO} mice exhibited prolonged running endurance as shown by significantly lower electric shock incidents (Extended Data Fig. 3j and Supplementary Videos 2 and 3). In line with those observations, a significant upregulation of mitochondrial respiration-related genes (Fig. 3q) along with a marked increase of mitochondrial copy numbers were noted in the *Kdm2a*^{SKO} mice (Extended Data Fig. 3k). TEM analysis of Gas sections further unveiled fewer swollen mitochondria and a higher density of mitochondrial cristae coupled with reduced lipid droplets in the *Kdm2a*^{SKO} mice (Fig. 3r).

To validate the above data, we further tackled the impact of *Kdm2a* on lipid stress in *Kdm2a*-deficient myotubes. Indeed, depletion of *Kdm2a* produced myotubes with significantly enhanced thermogenesis, as characterized by a marked decrease in ERthermAC intensity (a heat-sensitive fluorescent dye tailored for monitoring temperature fluctuations in thermogenic cells^{38,39}) following a 48 h palmitic acid challenge (Extended Data Fig. 3l). The enhanced thermogenesis was coupled with increased myoangiogenesis (Extended Data Fig. 3n) and STM transition (Extended Data Fig. 3m,n), enhanced mitochondrial biogenesis and oxidative respiration (Extended Data Fig. 3o,p). Taken together, our data support that loss of *Kdm2a* promotes an FTM-to-STM transition, thereby enhancing skeletal muscle metabolic flexibility to preferentially consume lipids and adapt to overnutrition-induced metabolic stress.

Kdm2a remodels lipid metabolism under an HFD challenge

To dissect the mechanisms by which *Kdm2a* regulates the transition of myofiber types, we conducted RNA deep sequencing of Gas muscle samples collected from HFD-challenged WT and *Kdm2a*^{SKO} male mice. Both Kyoto Encyclopedia of Genes and Genomes (KEGG) and Gene Ontology analyses characterized the pathways relevant to lipid metabolism (Fig. 4a,b). Specifically, KEGG analysis highlighted the enrichment of PI3K-AKT and AMPK signalling pathways, both of which are known to be linked to skeletal muscle fibre type transition (Fig. 4a). RT-qPCR analysis confirmed the expression changes of genes related to lipolysis and fatty acid oxidation (Fig. 4c) as well as lipogenesis (Fig. 4d). The decrease in the expression of glycolytic genes further confirmed that loss of *Kdm2a* in skeletal muscle promotes the transformation of the skeletal muscle metabolic pattern from glucose to lipid metabolism, which is achieved by reshaping skeletal muscle fibre types (Extended Data Fig. 4a). This is also consistent with the lower RER value of *Kdm2a*^{SKO} mice shown in Fig. 3k, which indicates preferential consumption of lipids as the main fuel for energy supply upon HFD induction. Notably, the *Kdm2a*^{SKO} mice exhibited significantly lower concentrations of triglycerides and total cholesterol (T-CHO) in the Gas tissues and circulation following either HFD challenge (Fig. 4e,f) or cold challenge (Fig. 4h,i) as well as in the serum levels of free fatty acids (Extended Data Fig. 4b,c), which was further corroborated by western blot analysis of markers (such as p-ACC and *Cpt1a*) relevant to lipolysis (Fig. 4g,j). Similar results were observed in C2C12 myotubes following palmitic acid or cold stimulation (Extended Data Fig. 4d,e). Those observations were consistent with the TEM results of attenuated lipid droplet accumulation in the Gas muscles from *Kdm2a*^{SKO} mice (Fig. 3r). Although normal-diet *Kdm2a*^{SKO} mice, after the completion of the cold challenge, showed consumption of glucose as the main fuel to maintain body temperature (Fig. 2j), the loss of *Kdm2a* also promoted the consumption of

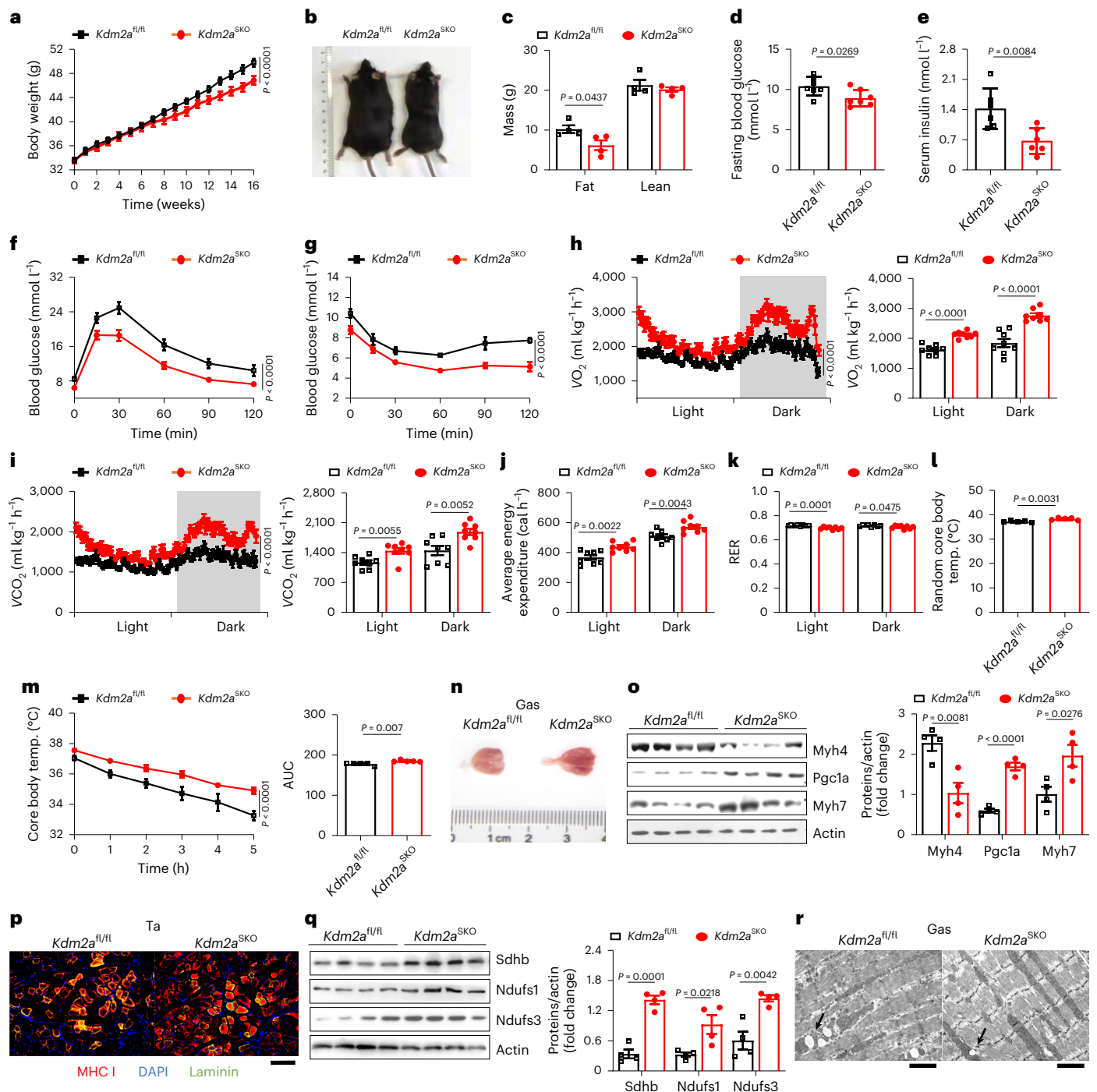


Fig. 3 | Loss of *Kdm2a* promotes lipid consumption in HFD-induced mice. **a**, Body weight of HFD *Kdm2a^{fl/fl}* and *Kdm2a^{SKO}* mice ($n = 7$ per group). **b**, Representative image of *Kdm2a^{fl/fl}* and *Kdm2a^{SKO}* mice after 16 weeks of a HFD challenge (right) ($n = 4$ per group). **c**, Weight of fat and lean mass of HFD *Kdm2a^{fl/fl}* and *Kdm2a^{SKO}* mice ($n = 4$ per group). **d**, Fasting blood glucose and **e**, serum insulin levels in *Kdm2a^{fl/fl}* and *Kdm2a^{SKO}* mice after 16 weeks of HFD ($n = 7$ per group). **f**, Intraperitoneal glucose tolerance test and **g**, insulin tolerance test of *Kdm2a^{fl/fl}* and *Kdm2a^{SKO}* mice after 16 weeks of HFD ($n = 6$ per group). **h–k**, Parameters measured in metabolic cages with HFD-fed *Kdm2a^{fl/fl}* and *Kdm2a^{SKO}* mice: oxygen consumption and quantification in the right panel (**h**), Carbon dioxide emission and quantification in the right panel (**i**), average energy expenditure (**j**) and RER (**k**) ($n = 8$ per group). **l**, Random core body temperature at room temperature of HFD-fed *Kdm2a^{fl/fl}* and *Kdm2a^{SKO}* mice ($n = 5$ per group). **m**, Core body temperature during fasting monitored with a cold challenge of HFD-fed *Kdm2a^{fl/fl}* and *Kdm2a^{SKO}*

mice ($n = 5$ per group). **n**, Representative image of HFD-fed *Kdm2a^{fl/fl}* (left) and *Kdm2a^{SKO}* (right) mice Gas tissue ($n = 5$ per group). **o**, Western blot analysis of Myh4, Pgc1a and Myh7 in Gas tissues from *Kdm2a^{fl/fl}* and *Kdm2a^{SKO}* mice fed with a HFD for 16 weeks ($n = 4$ per group). **p**, Representative immunostaining of Laminin (green), MHC I (red) and DAPI (blue) in Ta tissue cross sections from *Kdm2a^{fl/fl}* and *Kdm2a^{SKO}* mice. Scale bars, 100 μm ($n = 4$ per group). **q**, Western blot showing expression of mitochondrial biogenesis-related proteins (Sdhb, Ndufs1, Ndufs3) in HFD-fed *Kdm2a^{fl/fl}* and *Kdm2a^{SKO}* mice ($n = 4$ per group). **r**, Representative TEM images of Gas tissue cross sections from HFD-fed *Kdm2a^{fl/fl}* and *Kdm2a^{SKO}* mice. Lipid droplets were indicated by arrows. Scale bars, 20 μm ($n = 4$ per group). Data are expressed as mean \pm s.e.m. Statistical significance was assessed by two-way ANOVA (**a**, **f–i**, **m**) followed by Bonferroni's multiple comparisons test or two-sided Student's *t*-test (**c–e**, **j–l**, **o**, **q**).

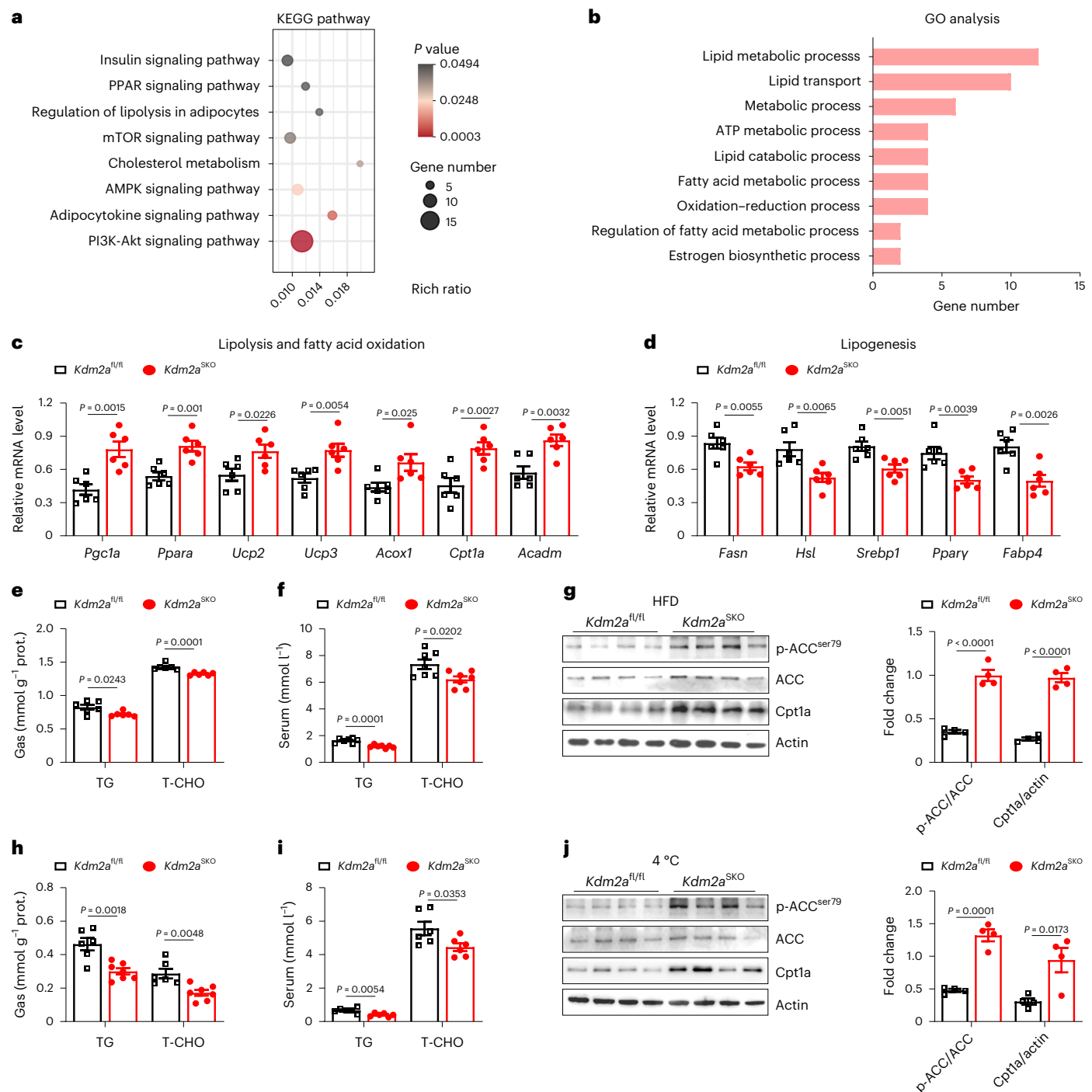


Fig. 4 | Kdm2a remodels lipid metabolism under HFD challenge. **a, b**, Gas tissues from HFD-fed *Kdm2a^{fl/fl}* and *Kdm2a^{SKO}* male mice were isolated and subjected to deep RNA-seq analysis. KEGG pathways (**a**) and Gene Ontology (GO) analysis (**b**) were generated from RNA deep sequencing data ($n = 3$ per group). **c**, RT-qPCR analysis of the expression of lipolysis and fatty acid oxidation-related genes in HFD-fed *Kdm2a^{fl/fl}* and *Kdm2a^{SKO}* male mice ($n = 6$ per group). **d**, RT-qPCR analysis of the expression of lipogenesis-related genes in HFD-fed *Kdm2a^{fl/fl}* and *Kdm2a^{SKO}* male mice ($n = 6$ per group). **e, f**, Triglyceride (TG) and T-CHO levels in Gas tissues (**e**) and serum (**f**) of HFD-fed *Kdm2a^{fl/fl}* and *Kdm2a^{SKO}*

male mice ($n = 6$ or 7 per group). **g**, Representative western blot analysis of lipolysis-related proteins (phosphorylated ACC and Cpt1a) in HFD-fed *Kdm2a^{fl/fl}* and *Kdm2a^{SKO}* male mice ($n = 4$ per group). **h, i**, TG and T-CHO levels in Gas tissues (**h**) and serum (**i**) of cold-adapted *Kdm2a^{fl/fl}* and *Kdm2a^{SKO}* male mice ($n = 6$ per group). **j**, Representative western blot analysis of lipolysis-related proteins (phosphorylated ACC and Cpt1a) in cold-adapted male mice ($n = 4$ per group). Data are expressed as mean \pm s.e.m. Two-sided unpaired Student's *t*-test was used for statistical analysis (**a**, **c**–**j**).

lipid fuel. Collectively, these findings support that *Kdm2a* deficiency reshapes skeletal muscle lipid metabolic profiles to induce a transition from FTM to STM, thereby enhancing energy consumption to promote thermogenesis and alleviate metabolic stress.

Esrrg pre-mRNA splicing reshapes muscle metabolic pattern
To elucidate how *Kdm2a* deficiency reshapes lipid metabolism in skeletal muscle, we conducted chromatin immunoprecipitation with sequencing (ChIP-seq) analysis, using Gas tissues obtained

from both HFD-fed *Kdm2a*^{SKO} and *Kdm2a*^{fl/fl} male mice. Interestingly, co-analysis of RNA sequencing (RNA-seq) and ChIP-seq data unveiled co-upregulation in the *Kdm2a*^{SKO} mice of estrogen-related receptor γ (*Esrrg*) (Fig. 5a), a well-recognized transcriptional activator of Pgc1a⁴⁰, which has a crucial role in lipid metabolism, myoangiogenesis and mitochondrial biogenesis in skeletal muscle^{41,42}. Western blotting and RT-qPCR analyses indeed confirmed a notable upregulation of *Esrrg* either in HFD-fed *Kdm2a*^{SKO} mice (Fig. 5b,c) or palmitic-acid-challenged *Kdm2a*-KO myotubes (Extended Data Fig. 5a,b). These results prompted us to tackle the impact of H3K36me2 on *Esrrg* expression. Motif analysis of H3K36me2 peaks revealed discrepant binding sites between H3K36me2 and *Esrrg*, primarily located in the intergenic intron regions. Specifically, H3K36me2 displayed significantly higher enrichments within the intron 5 region of *Esrrg* (188,170 kb to 188,190 kb) (Fig. 5d). ChIP-PCR further confirmed three highly enriched peaks: peak 35,364, peak 35,366 and peak 35,370 (Fig. 5d,e). Intriguingly, RT-qPCR analysis revealed a notable decrease in terms of RNA levels for the above three fragments in the Gas tissue of *Kdm2a*^{SKO} mice (Fig. 5f). These results imply that *Kdm2a* may catalyse H3K36me2 demethylation to regulate pre-mRNA splicing. To address this notion, primers were designed to cover the above three peaks located within intron 5 (F-intron5) and exons 4 and 5 (F-Exon4-5) (Extended Data Fig. 5d). RT-qPCR confirmed that *Kdm2a* deficiency (coupled with higher H3K36me2 levels) led to a significant increase in RNA levels for exons 4-5 but a marked decrease of intron 5 (Fig. 5g).

All exons of the five transcriptional variants of *Esrrg* are identical except for exon 1 and/or exon 2, as illustrated in Extended Data Fig. 5d,e. To dissect how H3K36me2 specifically regulates intron splicing and its potential impact on isoform formation, we designed primers targeting the common splicing regions of different isoforms and the adjacent common exon regions (F-intron1 and F-exon2-3). Moreover, primers were developed to cover the mature regions of each isoform (F-isoform1, F-isoform2, F-isoform3, F-isoform4 and F-isoform5). Additional primers were also designed to cover intron 2-6 regions (F-intron2, F-intron3, F-intron4 and F-intron6). RT-qPCR analysis revealed that intron splicing primarily occurred in the intron 5 region (Fig. 5h). Furthermore, different *Esrrg* isoforms exhibited a 1.7-fold to 1.9-fold increase compared to the WT mice (Fig. 5i). It is noteworthy that no significant difference was found between the WT and KO mice for the F-intron1/F-exon2-3 ratio (Fig. 5j), indicating that *Kdm2a* deficiency only selectively impacts the splicing of introns. In support of this notion, studies conducted in *Kdm2a*-KO C2C12 myotubes yielded consistent results (Extended Data Fig. 5c,f-i).

To further elucidate the involvement of H3K36me2 in *Esrrg* intronic splicing, mass spectrometry analysis after co-immunoprecipitation (co-IP) with an H3K36me2 antibody was carried out in C2C12 myotubes. Encouragingly, the data revealed a strong signal of the MORF-related gene on chromosome 15 (*Mrg15*) (Supplementary Fig. 3a). Previous reports have shown that H3K36me3

can recruit *Mrg15*, which can interact with polypyrimidine tract binding protein2 (PTBP2), thereby facilitating the engagement of the splicing machinery in the pre-mRNA splicing process^{43,44}. By detecting the levels of H3K36me3 in *Kdm2a*-KO myotubes (Supplementary Fig. 3b) and Gas tissues of *Kdm2a*^{SKO} mice (Supplementary Fig. 3c), the possible impact of H3K36me3 on *Mrg15*-mediated differential intron splicing was excluded. Western blot analysis of co-IP products confirmed a strong interaction between H3K36me2 and *Mrg15* in the *Kdm2a*-KO myotubes (Fig. 5k). Additionally, elevated binding levels were observed in the Gas tissues of *Kdm2a*^{SKO} mice (Fig. 5l). To confirm that H3K36me2 recruits *Mrg15*, which then promotes pre-mRNA maturation to enhance *Esrrg* expression, short interfering RNA designed to target *Mrg15* (si-*Mrg15* RNA) was transfected into the *Kdm2a*-KO myotubes. The si-*Mrg15* RNA induced a significant reduction in *Esrrg* expression (Fig. 5m and Extended Data Fig. 6a,b), and comparable H3K36me2 levels were noted between the *Kdm2a*-KO and si-*Mrg15* RNA transfected myotubes (Fig. 5m and Extended Data Fig. 6b). ERthermAC staining revealed an increased fluorescence intensity in si-*Mrg15* RNA transfected myotubes (Extended Data Fig. 6c), indicative of attenuated thermogenesis. Furthermore, knockdown of *Mrg15* reversed the phenotype of improved mitochondrial function (Extended Data Fig. 6f,g), increased STMs (Extended Data Fig. 6d,f) and enhanced lipid metabolism (Extended Data Fig. 6e,f) caused by *Kdm2a* deficiency. Similarly, knockdown of *Mrg15* expression reversed the basal and maximal mitochondrial oxygen consumption rates in *Kdm2a*-KO myotubes (Extended Data Fig. 6h), which was coupled with attenuated mitochondrial biogenesis (Extended Data Fig. 6f,g).

Next, a skeletal muscle-specific *Esrrg* knockdown model was generated in *Kdm2a*^{SKO} mice by using scAAVrh.74.MHCK7.Hesrrg particles (defined as *Kdm2a*^{SKO}-sh*Esrrg* mice). Injection of mice with self-complementary adeno-associated viruses (scAAVs) carrying shCTR was used as a control. The transduction efficiency was assessed through immunostaining (Extended Data Fig. 7a), and western blotting confirmed a significant reduction of *Esrrg* expression following 1 month of viral injection (Extended Data Fig. 7b). Cold challenge revealed that knockdown of *Esrrg* impaired the capability of *Kdm2a*^{SKO} mice to maintain the stability of their body temperature (Extended Data Fig. 7c), and decreased random body temperature was also noted at room temperature (Extended Data Fig. 7d). Their Gas muscles exhibited a reduced proportion of STMs (Fig. 5n) and were thus a much lighter colour (Extended Data Fig. 7e) along with attenuated mitochondrial biogenesis compared to the control mice (Extended Data Fig. 7f,g). TEM analysis also demonstrated decreased mitochondrial density (Fig. 5o). The *Kdm2a*^{SKO}-sh*Esrrg* mice manifested impaired lipolysis (Extended Data Fig. 7h) accompanied by an increase of triglyceride and T-CHO levels in the serum and tissues (Extended Data Fig. 7i). These findings were also corroborated by in vitro reversal experiments, in which si-*Esrrg* RNA was transfected into the *Kdm2a*-KO myotubes. Knockdown of *Esrrg* did not impact the H3K36me2 levels

Fig. 5 | *Esrrg* pre-mRNA splicing reshapes muscle metabolic pattern.

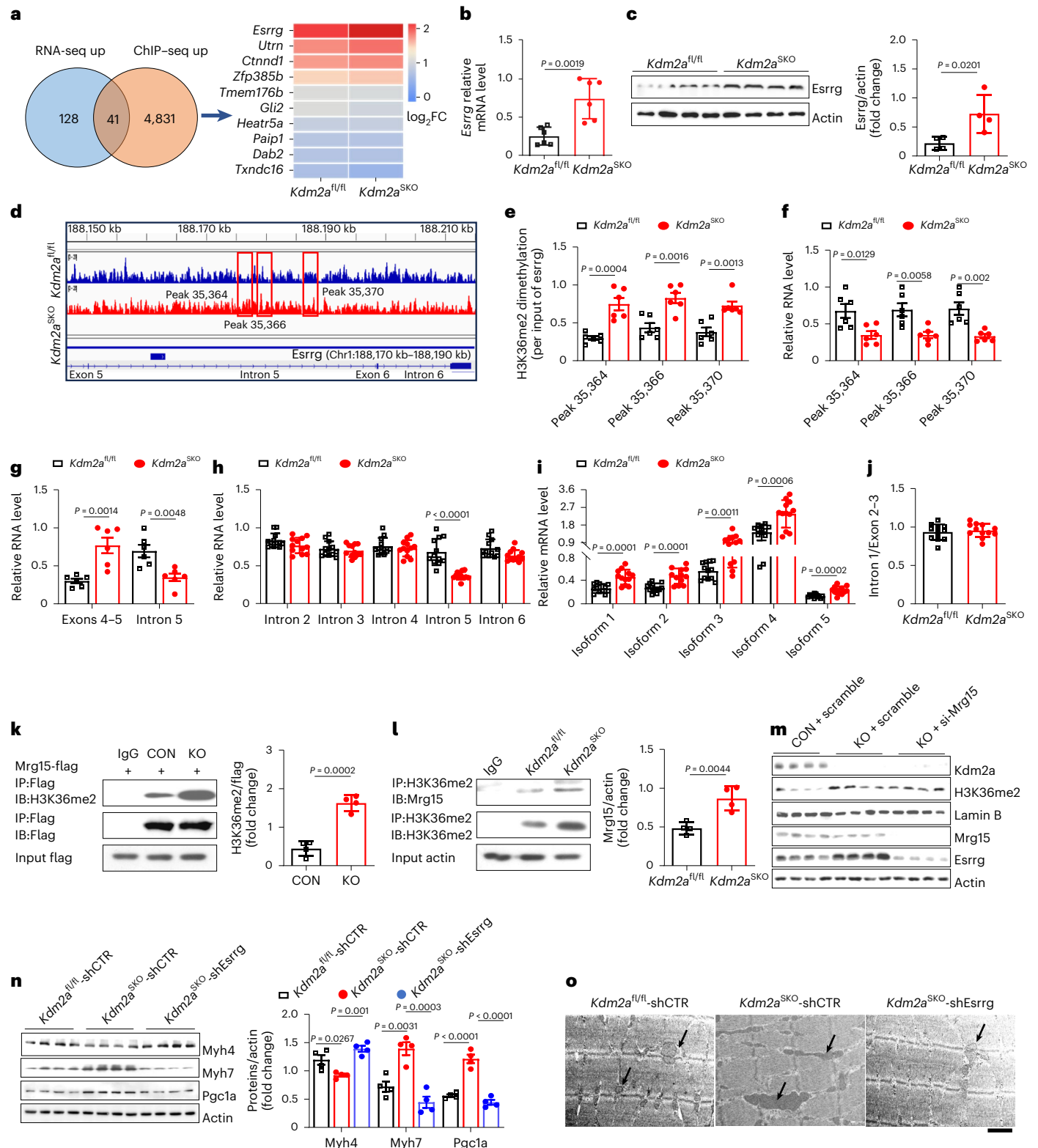
a, ChIP-seq of isolated Gas tissue from HFD-fed *Kdm2a*^{fl/fl} and *Kdm2a*^{SKO} mice. Venn diagram showing co-upregulated genes revealed by RNA-seq and ChIP-seq (left), and heatmap showing the differentially expressed genes (right) ($n = 3$ per group). FC, fold change. **b**, RT-qPCR ($n = 6$ per group) and **c**, western blot analysis ($n = 4$ per group) of *Esrrg* expression levels in Gas tissue from HFD-fed *Kdm2a*^{fl/fl} and *Kdm2a*^{SKO} mice. **d**, ChIP-seq analysis of the *Esrrg* locus showing the peak locations relative to the intron ($n = 3$ per group). **e**, ChIP-qPCR analysis showing intron fragments marked by H3K36me2 in Gas tissue from HFD *Kdm2a*^{fl/fl} and *Kdm2a*^{SKO} mice ($n = 6$ per group). **f**, RT-qPCR analysis of transcribed *Esrrg* intron fragments in Gas tissue from HFD-fed *Kdm2a*^{fl/fl} and *Kdm2a*^{SKO} mice ($n = 6$ per group). **g**, Relative RNA levels of transcribed *Esrrg* exons 4-5 and intron 5 between Gas tissue from HFD-fed *Kdm2a*^{fl/fl} and *Kdm2a*^{SKO} mice ($n = 6$ per group). **h**, Relative RNA levels of transcribed *Esrrg* introns between Gas tissue from HFD-fed *Kdm2a*^{fl/fl} and *Kdm2a*^{SKO} mice ($n = 12$ per group). **i**, Relative expression of different isoforms of *Esrrg* between Gas tissue from HFD-fed *Kdm2a*^{fl/fl} and *Kdm2a*^{SKO} mice

($n = 12$ per group). **j**, The transcribed ratio of intron 1 to exons 2-3 in Gas tissue from HFD-fed *Kdm2a*^{fl/fl} and *Kdm2a*^{SKO} mice ($n = 12$ per group). **k**, Transfection of C2C12 myotubes with *Mrg15-Flag* expressing plasmids. Immunoprecipitated *Mrg15-Flag* was probed for H3K36me2 using an anti-H3K36me2 antibody. The quantification is in the right panel ($n = 4$ per group). **l**, In HFD *Kdm2a*^{fl/fl} and *Kdm2a*^{SKO} mice Gas tissue, immunoprecipitated H3K36me2 was probed for *Mrg15* using an anti-*Mrg15* antibody. The quantification is in the right panel ($n = 4$ per group). **m**, Western blot measurement of *Mrg15*, H3K36me2, *Kdm2a* and *Esrrg* expression levels in C2C12 myotubes ($n = 4$ per group). **n-o**, Male mouse model of skeletal muscle-specific *Esrrg* knockdown, **(n)** detected Pgc1a, Myh4 and Myh7 protein levels and **(o)** the representative TEM images of Gas from *Kdm2a*^{fl/fl}-shCTR, *Kdm2a*^{SKO}-shCTR and *Kdm2a*^{SKO}-sh*Esrrg* mice ($n = 4$ per group). Mitochondria are indicated by arrows. Scale bars, 10 μ m. Data are expressed as mean \pm s.e.m. Statistical significance was assessed by two-sided Student's *t*-test (**b**, **c**, **e-n**).

(Supplementary Fig. 4a) but reversed the phenotypes that resulted from *Kdm2a* deficiency, such as thermogenesis (Supplementary Fig. 4b), lipid metabolic patterns (Supplementary Fig. 4e,f), STM transition (Supplementary Fig. 4d,f) and mitochondrial function (Supplementary Fig. 4c,f).

The above observations prompted us to examine *Esrrg* expression profiles in both cold-challenged (Extended Data Fig. 7j) and HFD-challenged (Extended Data Fig. 7k) WT mice; its expression levels were positively correlated with H3K36me2 levels (Fig. 1c,e). Similar

results were recapitulated in experiments with myotubes (Extended Data Fig. 7l,m). Importantly, studies in human muscle samples also confirmed that subjects with a higher BMI exhibited lower ESRRG levels (Extended Data Fig. 7n), and *ESRRG* mRNA was negatively correlated with *KDM2A* expression (Extended Data Fig. 7o), further confirming that *Esrrg* is a *Kdm2a* downstream target. Taken together, our data support that loss of *Kdm2a* promotes the formation of an H3K36me2–Mrg15 complex, thereby enhancing *Esrrg* pre-mRNA splicing to increase its expression.



Kdm2a could be a viable target against metabolic stress

Finally, we sought to check the feasibility of Kdm2a as a target against metabolic stress in clinical settings. Daminozide, a KDM2A inhibitor, was used for the study. WT 8-week-old male mice were fed a HFD for 16 weeks to induce obesity and insulin resistance. These mice were maintained on a HFD but subjected to sustained cold challenge for 2 weeks, and daminozide was administered by intraperitoneal injection at 50 mg kg⁻¹ day⁻¹ or 100 mg kg⁻¹ day⁻¹ or the same volume of PBS, respectively. The mice were then housed under normal temperature with a HFD for at least 24 h before the following assessments. It was noted that daminozide caused the mice to have a significantly higher random core body temperature (Extended Data Fig. 8a) and percentage of body weight loss (Extended Data Fig. 8b). Consistently, those mice exhibited significantly improved fasting blood glucose levels (Extended Data Fig. 8c), glucose tolerance (Extended Data Fig. 8d) and insulin sensitivity (Extended Data Fig. 8e). However, no dose-dependent effect was observed; therefore, we next primarily focused on those mice treated with a low dose of daminozide. In line with the above observations, metabolic assays revealed that the daminozide-treated mice displayed markedly higher rates of oxygen consumption (Fig. 6a), carbon dioxide emission (Fig. 6b) and energy consumption (Fig. 6c), along with enhanced β -oxidation as they exhibited much lower RER (Fig. 6d); no discernible difference in terms of diet and water intake was noted (Extended Data Fig. 8f). We then challenged the mice with a cold insult again and noted that the daminozide-treated mice manifested a significantly higher capability to maintain their core body temperature stability (Fig. 6e and Extended Data Fig. 8g).

To further validate the effect of daminozide treatment, skeletal muscles were isolated for additional analysis. Unlike the controls, the Gas tissues that originated from daminozide-treated mice were dark red, indicating highly enriched mitochondria and Mb content (Fig. 6f). Although we failed to detect a marked difference in muscle mass (Extended Data Fig. 8h), enhanced FTM-to-STM transition was noted (Fig. 6g,h and Extended Data Fig. 8i). Significantly improved mitochondrial oxidative respiration (Fig. 6i) and biogenesis (Fig. 6j) were also detected. Moreover, TEM analyses revealed increased mitochondrial numbers and cristae density in the skeletal muscle sections along with decreased lipid droplets (Fig. 6k). Consistent with these observations, genes relevant to lipid metabolism were highly expressed following daminozide treatment (Fig. 6l,m), which was coupled with decreased triglyceride and T-CHO levels both in the serum (Extended Data Fig. 8j) and Gas tissues (Fig. 6n). These findings collectively demonstrate that daminozide enhances energy consumption and reshapes skeletal muscle lipid metabolic patterns under conditions of overnutrition. Of note, daminozide itself did not affect *Kdm2a* expression but led to a significant upregulation of H3K36me2 levels (Fig. 6p), thereby enhancing *Esrrg* mRNA expression (Fig. 6o) to increase its protein levels (Fig. 6p). Furthermore, RT-qPCR confirmed a decrease in expression in fragments (peak 35,364, peak 35,366, peak 35,370) (Extended Data Fig. 8k), along with increased F-exon4–5 but decreased F-intron5 expressions (Fig. 6q), demonstrating that daminozide promotes *Esrrg*

expression by facilitating its intronic splicing. In conclusion, daminozide manifested a pronounced capacity to reprogramme skeletal muscle metabolic profiles from glycolysis to β -oxidation upon the challenge of overnutrition, whereby it augmented energy consumption against metabolic stress, thereby supporting that Kdm2a could be a viable target against metabolic stress in clinical settings.

Discussion

Chronic overnutrition caused by daily diet is commonly coupled with an excessive accumulation of mixed fuels, predisposing the development of metabolic stress⁴⁵. As the largest metabolic organ in the body, skeletal muscle possesses the flexibility to selectively consume certain types of fuels to adapt to the metabolic stress resulting from overnutrition^{8,46}. However, this adaptive mechanism is generally impaired during the development of obesity. In particular, skeletal muscle exhibits decreased mitochondria mass and impaired function coupled with a marked reduction of the proportion of STM in obese conditions^{11,47–50}. PTMs of histone proteins, especially histone 3 methylations, a typical epigenetic factor, are thought to be highly involved, but the exact regulatory mechanisms are yet to be fully elucidated. Therefore, in the current study, we used an inducible skeletal muscle-specific *Kdm2a* knockout model (that is, *Kdm2a*^{SKO} mice) and daminozide, an inhibitor for demethylase Kdm2a, to address the impact of H3K36me2 on the regulation of skeletal muscle metabolic flexibility upon the insult of metabolic stress. Kdm2a is highly expressed in FTMs and negatively correlated with H3K36me2 levels in mouse skeletal muscle. Similarly, *KDM2A* mRNA levels in the human tibialis anterior muscle are positively correlated with BMI but with attenuated PGC1a expressions, a marker relevant to energy consumption and mitochondrial biogenesis²⁸. Mice deficient in *Kdm2a* exhibited a higher capability against cold challenge and were protected from HFD-induced obesity and insulin resistance. In general, *Kdm2a*^{SKO} mice preferentially consumed lipids upon the insult of overnutrition and exhibited a predominant consumption of glucose under a normal diet. Intriguingly, the improved metabolic flexibility in skeletal muscle caused by *Kdm2a* deficiency was achieved by inducing a FTM-to-STM transition by regulating *Esrrg* RNA splicing.

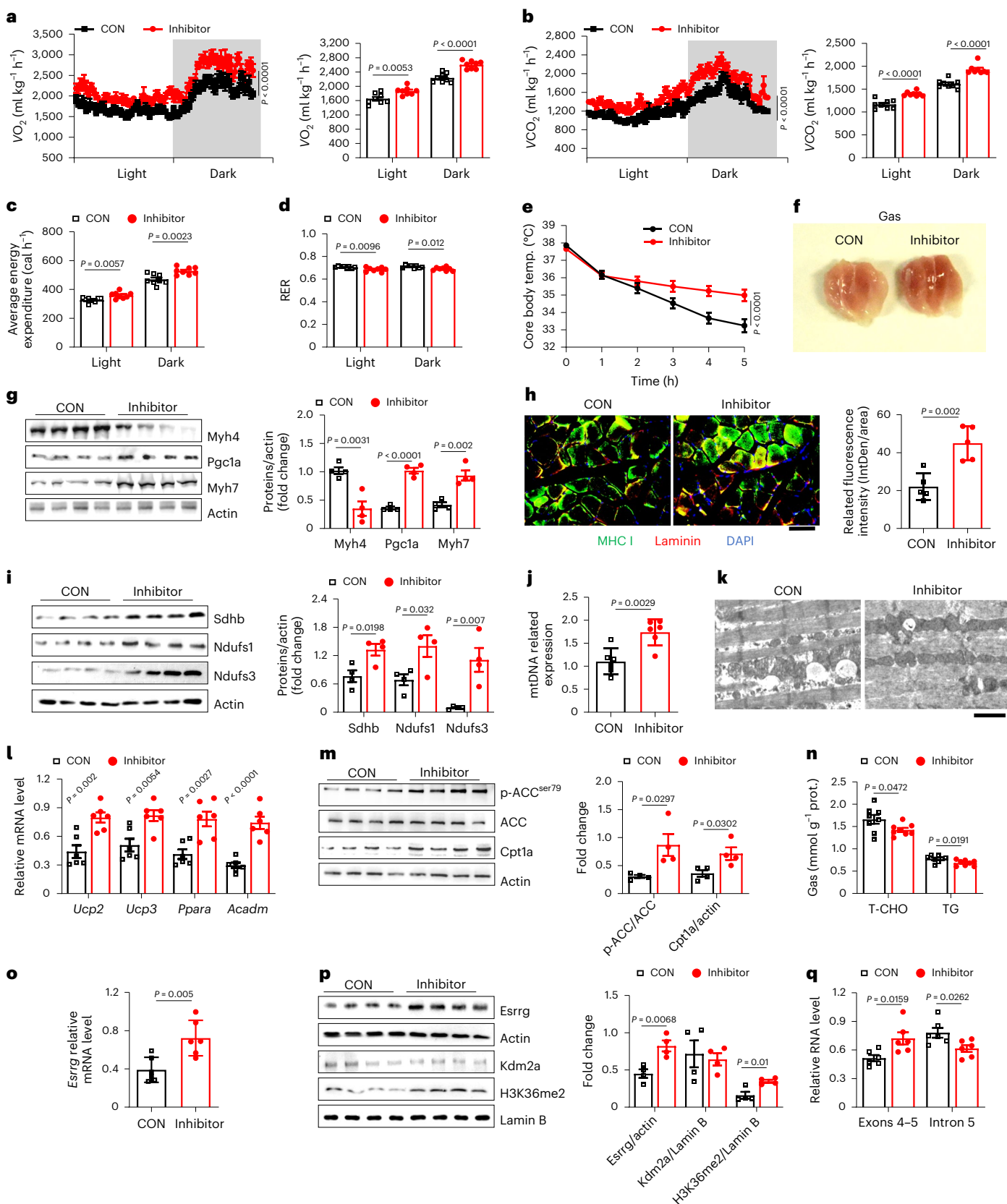
Metabolic flexibility in skeletal muscle has long been recognized as being relevant to the capacity of the human body to maintain metabolic homeostasis, but the underlying mechanisms have yet to be fully addressed. Our data demonstrate experimental evidence supporting that the metabolic flexibility in skeletal muscle is probably determined by a switch in energy consumption under different conditions, such as the consumption of glucose, lipids, glycogen and amino acids. Indeed, previous studies have suggested feasible evidence that the type of exercise affects the absorption and use of fuels by skeletal muscle, thereby reshaping its metabolic style^{8,51}. Specifically, short-term exercise consumes considerable glucose and glycogen, while long endurance and resistance exercise require the use of fatty acid oxidation for energy demand^{52–54}. Similarly, undernutrition or overnutrition exerts a profound effect on skeletal muscle metabolism by altering fuel use, fuel handling and storage capacity⁵⁵. In line with those observations,

Fig. 6 | Kdm2a could be a viable target against metabolic stress. a–d, Detection of oxygen consumption (a) and carbon dioxide emission (b), with quantification in the right panels, (c) average energy expenditure and (d) RER during light and dark conditions in metabolic cages ($n = 8$ per group). CON, PBS control; inhibitor, diaminozide treatment. e, Core body temperature of control and inhibitor groups ($n = 7$ per group) at 4 °C. f, Representative Gas photograph from control and inhibitor groups ($n = 4$ per group). g, Western blot ($n = 4$ per group) analysis of Myh4, Pgc1a and Myh7 expression in control and inhibitor groups. h, Representative immunostaining of Laminin (red), MHC I (green) and DAPI (blue) in frozen sections of control and inhibitor group Ta. Scale bars: 50 μ m ($n = 5$ per group). i, Western blot analysis of Sdhb, Ndufs1, Ndufs3 expression in control and inhibitor groups ($n = 4$ per group). j, mtDNA copy number in control and inhibitor groups ($n = 6$ per group). k, Representative TEM images in control and

inhibitor group Ta. Scale bars, 5 μ m, $n = 4$ per group. l, RT-qPCR analysis of *Ucp2*, *Ucp3*, *Ppara* and *Acadm* expression in control and inhibitor group mice ($n = 6$ per group). m, Western blot analysis of p-ACC/ACC and Cpt1a levels in control and inhibitor group mice ($n = 4$ per group). n, TG and T-CHO content Gas tissue from control and inhibitor group mice ($n = 8$ per group). o, RT-qPCR analysis of *Esrrg* levels in Gas tissue of control and inhibitor group mice ($n = 6$ per group). p, Western blot measurement of H3K36me2, Kdm2a and *Esrrg* expression levels in control and inhibitor group mice ($n = 4$ per group). q, Relative RNA levels of transcribed exons 4–5 and intron 5 fragments in control and inhibitor group mice ($n = 6$ per group). Data are expressed as mean \pm s.e.m. Statistical significance was assessed by two-way ANOVA (a, b, e) followed by Bonferroni's multiple comparisons test or two-sided Student's *t*-test (a–d, g–j, l–q).

conditions such as sepsis, cachexia, metabolic acidosis, ageing and diabetes are often coupled with muscle atrophy accompanied by elevated amino acid catabolism in skeletal muscle^{56–58}. Our studies support that H3K36me2 levels are a key factor underlying the regulatory mechanisms. In particular, *Kdm2a*^{SKO} mice exhibited a significantly

higher RER than WT mice on a normal diet, and the RER was markedly reduced following a HFD challenge. These findings support that the elevated H3K36me2 levels resulting from *Kdm2a* deficiency allow skeletal muscle to facilitate a rapid shift from glucose to lipid use upon the insult of metabolic stress, thereby enhancing its metabolic flexibility



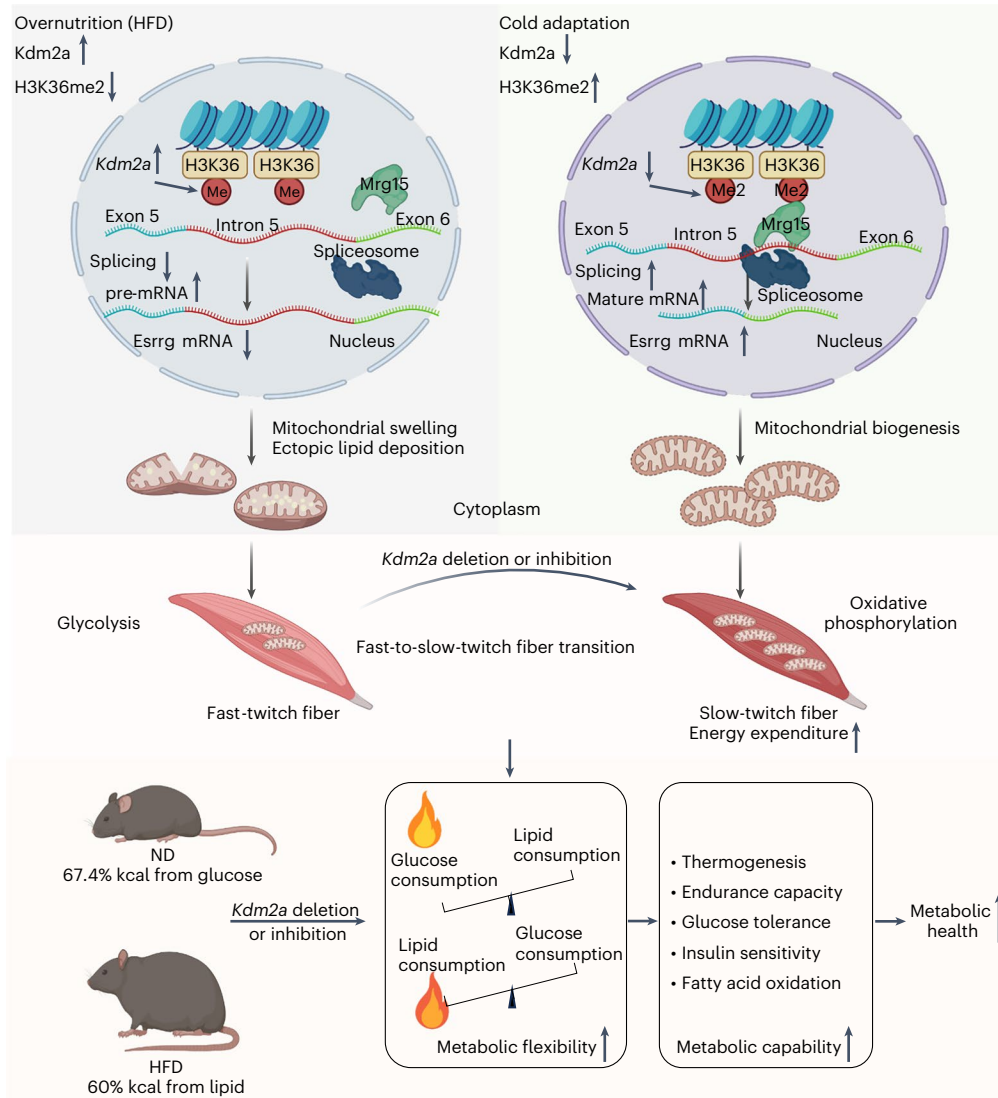


Fig. 7 | *Kdm2a* deficiency reshapes muscle metabolic flexibility. Inhibition of *Kdm2a* provides skeletal muscles with enhanced metabolic flexibility to shift fuel use from glucose as the main energy source under a normal diet accompanied by cold challenge to lipids as the main energy source under obese condition by

increasing the proportion of STMs, which then enhances the capability of the mice to withstand metabolic stress. These insights hold significant implications for *Kdm2a* to serve as a viable target against metabolic stress in clinical settings (made with BioRender.com).

to prevent the excessive accumulation of mixed fuels. It is noteworthy that metabolic flexibility has been largely proposed as being a beneficial factor, although conflicting effects could also occur under certain conditions. For example, electron transport chain dysfunction leads to excessive hepatic lipid deposition, deletion of pyruvate dehydrogenase 4 (*Pdk4*) allows pyruvate oxidation to acetyl-CoA and this metabolic inflexibility promotes improvements in mitochondrial health during liver regeneration⁵⁹. Therefore, the identification of targets capable of regulating skeletal muscle metabolic flexibility may pave the way to develop viable strategies against metabolic disorders in different clinical settings.

Histone modifications, an epigenetic factor, are now recognized to have a crucial role in the regulation of metabolic flexibility in skeletal muscle. Typically, endurance exercise increases the cytoplasmic translocation of histone deacetylase 4 (HDAC4) and HDAC5 to enhance the activity of a myogenic transcription factor, MEF2, which then transcribes genes to improve running performance and reduce muscle fatigue^{60–62}. Nevertheless, the impact of histone methylations on the regulation of metabolic flexibility in skeletal muscle is mostly unresolved. Herein, we found that depletion

of *Kdm2a*, an enzyme highly expressed in FTMs to specifically catalyze the demethylation of H3K36me2, significantly improves the capacity of mice to withstand endurance exercise by targeting *Esrrg* to promote mitochondrial biogenesis. The correlation between *KDM2A* activity and *ESRRG* expression was also confirmed in human tibialis anterior muscle samples. Our data support that H3K36me2 levels in the skeletal muscle could be a critical marker to manifest the capacity of a particular individual to adapt to the challenge of metabolic stress.

Upon identification of the first methyltransferase responsible for the methylation of specific residues in the histone tails⁶³, follow-up studies opened the door to characterize many such enzymes and eventually led to the identification of many related histone demethylases⁶⁴. Other than methylation, a plethora of PTMs have also been identified on histones to date, such as acetylation, phosphorylation, SUMOylation, ubiquitination, succinylation, butyrylation and others^{64,65}. Of note, histone lysine methyltransferases are very dedicated enzymes, with enzymatic machinery devoted to the methylation of a specific lysine residue on a specific histone⁶⁶. We obtained a similar result for *Kdm2a*, a histone demethylase specifically upregulated in FTMs upon

the insult of metabolic stress. In general, histone methylations are relevant to chromatin remodelling associated with gene transcription or repression. However, studies have also suggested feasible evidence for a role in RNA slicing, such as H3K36 possibly impacting RNA alternative splicing⁶⁷. Herein, we demonstrated experimental evidence that the elevated H3K36me2 levels resulting from *Kdm2a* depletion regulate *Esrrg* RNA splicing, which is only limited to the splicing of introns; no perceptible impact was noted on the alternatively spliced isoforms. Of note, non-histone proteins have also been recognized to be methylated by the methyltransferases under certain conditions⁶⁸; therefore, whether *Kdm2a* regulates the methylation of non-histone proteins in the setting of metabolic stress would be a major focus for our follow-up studies.

As mentioned earlier, modern diets are commonly coupled with chronic overnutrition. A constant mix of fuel inputs along with a sedentary lifestyle further exacerbates the imbalance between energy intake and expenditure, ultimately leading to mitochondrial dysfunction⁴⁵. Our study showed that normal-diet *Kdm2a*^{SKO} mice preferentially consumed glucose to maintain their body temperature during a cold challenge (Fig. 2d,j and Extended Data Fig. 2l) and also used fatty acids as an energy substrate to avoid hypoglycemia and to better cope with the cold challenge (Fig. 4h–j and Extended Data Fig. 4c, e). Intriguingly, under high-fat-diet-induced nutritional stress, the muscular deletion of *Kdm2a* prioritized lipids over glucose as the major energy substrate by strengthening the functional capacity of mitochondria (Figs. 3k,q,r and 4e–g and Extended Data Fig. 4b,d). Overall, *Kdm2a* deficiency in skeletal muscle can flexibly adjust the priority of fuel use, thereby ensuring efficient adaptation to distinct stress conditions.

Conclusion

In summary, our study underscores a pivotal role for *Kdm2a*-mediated demethylation of H3K36me2 in the FTM–STM transition and reshaping skeletal muscle metabolic flexibility (Fig. 7). Inhibition of KDM2A provides skeletal muscles with enhanced metabolic flexibility to switch fuel consumption and to augment thermogenesis and energy expenditure upon the challenge of metabolic stress. These insights hold significant implications for comprehending the interplay between epigenetic regulation of metabolic pathways in skeletal muscle and offer a promising avenue for the intervention and management of metabolic disorders in clinical settings.

Methods

Mice

The *Kdm2a*^{fllox/fllox} (*Kdm2a*^{fl/fl}) mice in the C57BL/6 background were generated by targeting exons 7–9 (encoding the JmjC-catalytic domain) using a Cre-LoxP system. The Flp transgenic mice and ACTA1-rtTA, tetO-cre mice were purchased from the Jackson Laboratory (strain no. 012433). C57BL/6 (WT) mice were purchased from Beijing HFK Bioscience. All mice were maintained under specific-pathogen-free conditions at the Tongji Hospital Animal Center at 20–24 °C ambient temperature, 45–65% humidity and a 12/12 h light/dark cycle. Both ACTA1-rtTA, tetO-cre-*Kdm2a*^{fl/fl} (referred to as knockout (*Kdm2a*^{SKO})) mice and their *Kdm2a*^{fl/fl} littermates (referred to as WT (*Kdm2a*^{fl/fl})) controls) (8 weeks old) were either maintained on a normal diet (67.4% kcal from glucose, 11.1% kcal from lipid; Xietong Pharmaceutical Bio-engineering) or switched to a HFD (25.9% kcal from glucose, 60% kcal from fat; Research Diet) for 16 consecutive weeks. Mice were allocated to the normal diet or HFD groups randomly. *Kdm2a* deficiency was induced by drinking 2 mg ml⁻¹ of tetracycline (in 5% glucose) for 1 week. At the end of the experiment, the mice were killed for subsequent biochemical experiments. All experimental procedures were approved by the Tongji Hospital Animal Care and Use Committee in accordance with the National Institutes of Health guidelines (TJH-202204022).

Mouse hyperglycemic model

WT mice (8 weeks old) were randomly provided with normal drinking water or water containing 10% glucose for 2 weeks and then monitored for random blood glucose levels twice per week to make sure the mice were hyperglycemic (>16.7 mmol l⁻¹).

Human samples

Muscle samples from patients undergoing anterior cruciate ligament repair for anterior cruciate ligament rupture were collected at the Union Hospital of Tongji Medical College between 2018 and 2019. Clinical characteristics such as sex, height, age and BMI of each subject are summarized in Supplementary Table 1. None of the patients had significant systemic disease, chronic infection or previous history of myocardial infarction. Each subject received a consent form. All studies related to humans were conducted in accordance with National Institutes of Health guidelines and approved by the Institutional Review Board (IRB) of Tongji Hospital (TJ-IRB20230926).

Histone protein extraction

Histone proteins from STMs (soleus) and FTMs (extensor digitorum longus) were extracted using the EpiQuik Total Histone Extraction Kit (OP-0006, Epigentek). The protein concentration was quantified using a BCA kit (G2026, Servicebio).

High-glucose stimulation of C2C12 myotubes

C2C12 myotubes were pretreated with DMEM supplemented with low glucose (5.6 mmol l⁻¹) overnight. They were next washed with PBS and resuspended with fresh DMEM in the presence of low glucose or high glucose (30 mmol l⁻¹), respectively. After another 48 h of culture, the cells were collected for protein extraction.

Intraperitoneal glucose tolerance test and insulin tolerance test assays

For the intraperitoneal glucose tolerance test, the mice were fasted for 16 h before intraperitoneal injection of 15% glucose (w/v) at a dose of 1.5 g kg⁻¹ of body weight. The insulin tolerance test was conducted after 6 h of fasting and injected intraperitoneally with human regular insulin (Novolin R, Novo Nordisk) at 0.5 IU kg⁻¹ of body weight. Blood glucose was measured from tail vein blood at indicated time points using a glucometer (Roche). Serum insulin and fasting blood glucose were assayed at 16 h of fasting.

Cold adaptation and body temperature monitoring

To eliminate the effects of skeletal muscle shivering thermogenesis, a cold adaptation model was established, in which the mice were successively adapted to 18°C, 14°C, 10°C and 6°C for 1 week, respectively. Subsequently, the mice were placed in a cold room at 4–5°C for 8 h each day for 2 weeks (Supplementary Fig. 1f). After fasting for 6 h, core body temperature was measured under cold challenge with one mouse per cage. Random core body temperature was monitored at room temperature without restricting food intake. Additionally, some mice were placed in the prone position after intraperitoneal injection with 1.25% Avertin (M2920, Nanjing Aibei Biotechnology). After 30 min, core body temperature was measured using a rectal probe. The mice were then placed on a heating pad until they were fully awake. For studies in myocytes, C2C12 myotubes were placed in the 4°C cold room for 30 min and then returned to the cell incubator for 5 min. The cells were repeated four times for a total of 2 h of cold stimulation before the follow-up studies.

Histological and immunofluorescence staining

Tissue cross sections from skeletal muscle were prepared and subjected to hematoxylin and eosin staining. The stained sections were analysed under a Leica ST5010 Autostainer XL microscope (Leica Biosystems) by two pathologists in a blinded fashion. For immunostaining, mouse

skeletal muscles were removed at indicated time points. Tissue sections were prepared and placed in OCT, frozen in dry-ice-cooled isopentane (Tissue-Tek), fixed in 4% paraformaldehyde and blocked in 3% BSA in Tris-buffered saline. The sections were then incubated overnight at 4 °C with antibodies against major histocompatibility complex I and II and Laminin alpha 2 or KDM2A and α -SMA or CD31 and Laminin alpha 2, followed by probing with an AlexaFluor 488-conjugated anti-mouse IgG or an AlexaFluor 594-conjugated anti-rabbit IgG secondary antibody (Jackson ImmunoResearch Laboratories) for 1 h at room temperature. The slides were further stained with DAPI and then sealed with Vectashield. The immunofluorescence images were captured under a fluorescence microscope (Leica).

Western blotting

Lysates from skeletal muscle and C2C12 cells were prepared in RIPA buffer (Servicebio) and then subjected to western blot analysis. The specific information of each antibody is summarized in the Reporting Summary and the Key Source Table.

Body composition measurement

Body composition (lean and fat mass) was analysed using Bruker's Minispec Whole Body Composition Analyzer (Minispec LF 90II) based on TD-NMR.

Metabolic studies

The mice were housed individually in metabolic cages (Columbus Instruments) and given free access to food and water. After acclimation in the respiratory chambers for 24 h, the mice were monitored in real-time for 72 h for food and water intake, oxygen consumption, carbon dioxide production, RER and energy expenditure data as previously reported²³. All data were obtained and calculated by the Oxymax software.

Glucose uptake assay

Glucose uptake was measured using a Glucose Uptake Fluorometric Assay Kit (E-BC-F041, Elabscience), following the manufacturer's instructions. C2C12 myotubes were washed with PBS and starved in serum-free DMEM overnight. The cells were subsequently washed twice with KRPH containing 2% BSA and then incubated with 2-DG (10 mmol l⁻¹) for 30 min at 37 °C, followed by washing the cells three times with KRPH (pH 7.4). Next, reagent 1 was added into each well and incubated for 10 min at room temperature and then mixed with the same volume of reagent 2. The samples were then mixed with working solutions and incubated for 30 min at 37 °C. The fluorescent intensity was finally measured using a microplate reader (Synergy 2, Bio Tek) at excitation/emission = 530 nm/590 nm and normalized to protein concentration using a BCA kit. Relative glucose uptake was assessed according to the standard curve based on determination of the standard sample.

Biochemical and ELISA analysis

Skeletal muscle tissues or serum T-CHO and triglyceride levels and serum free fatty acids were measured with a biochemical auto-analyser (BS-200). The concentration of hepatic triglyceride was determined using a triglyceride assay kit (A110-1-1, Nanjing Jiancheng Bioengineering Institute) following the manufacturer's instructions.

C2C12 myoblasts culture and differentiation, transfection of plasmids and siRNAs

C2C12 myoblasts were obtained from ATCC (CRL-1772). Myoblasts were maintained in culture at <80% confluence in DMEM (high glucose) and 10% FBS. For differentiation, myoblasts were cultured at high-glucose DMEM with 1% horse serum. Myotube formation was monitored visually for 7–10 days before experimental use. C2C12 myoblasts were routinely tested and authenticated as negative for mycoplasma contamination.

Differentiated myotubes were transfected with RNAi oligonucleotides or negative-control siRNA using the Lipofectamine 3000 Transfection Reagent (L3000-015; Invitrogen) in Gibco Opti-MEM with 1% horse serum media. After washes following 18 h of transfection, the cells were resuspended in high-glucose DMEM supplemented with 1% horse serum and 1% penicillin–streptomycin and were ready for experimental use after 48 h of transfection. The Mouse *Mrg15* cDNA (NP_001034236) was directly synthesized by inserting a Flag tag after the carboxy-terminal sequence. The cDNA product was inserted into a pcDNA3.1 vector. *Mrg15*-Flag plasmids were transfected into C2C12 myotubes using the Lipofectamine 3000 and P3000 Transfection Reagent in high-glucose DMEM with 1% horse serum media. After washes following 12 h of transfection, the myotubes were ready for experimental use after 48 h of transfection. The related sequences are listed in Supplementary Table 3.

Generation of *Kdm2a*-KO C2C12 cells

Kdm2a knockout myoblasts (*Kdm2a*-KO) were generated using LentiCRISPR (v.2) containing a single guide RNA (gRNA). The sequence for LentiCRISPR (v.2) *Kdm2a* gRNA can be found in Supplementary Table 3. Lentivirus was packaged in C2C12 myoblasts by transient transfection. Conditioned media containing lentivirus was used to transduce C2C12 myoblasts. The cells were selected with puromycin and individual clones were characterized. *Kdm2a* deletion was verified by western blotting (Extended Data Fig. 2k) and gene sequencing (Supplementary Table 4).

Endurance running capacity and acute exercise test

The mice were acclimated to the treadmill (ZS-PT-III, Zhongshi) for three consecutive days at low speed (5 m min⁻¹) with no incline for 5 min. Running tests were performed with a 5° incline. Animals ran at 10 m min⁻¹ for the first 10 min followed by increases of 2 m min⁻¹ every 5 min until exhaustion, which was defined by the inability to remain on the treadmill for >5 s⁶⁹. Animals were removed immediately after exhaustion. For an acute exercise test, the mice were acclimated to treadmill running as outlined above. Animals were fasted for 4 h before single bouts of acute exercise set for 30 min at 12 m min⁻¹ with a 5° incline, and the electric shock incidents (the number of times the mice were electrically stimulated on a treadmill before exhaustion) were recorded.

RT-qPCR analysis

Total RNA was extracted from cells or tissues using the Trizol reagent (9109, Takara, Kusatsu-Shiga). The quantity and quality of RNA were determined using the Nano-drop 2000 (Thermo Scientific). Approximately 500 ng of RNA was used for reverse transcription using the HiScript II Q Select RT SuperMix (Vazyme). The cDNA was diluted 1:10 with nuclease-free water and used for real-time PCR on a QuantStudio 12K Flex (Life Technologies) using the SYBR qPCR Mix (Takara, Kusatsu-Shiga). The data were normalized to β -actin and analysed using the $\Delta\Delta C_t$ method as previously described⁷⁰. RNA extraction from intron detection groups and reverse transcription used the kits containing random hexamer primers (R212-01/02, Vazyme). Relative mitochondrial DNA was quantified by real-time PCR using primers for mitochondrially encoded Nd1 normalized to nuclear-encoded 36B4 (Rplp0) DNA. Relative expression levels were quantified using a standard curve and normalized to the expression of housekeeping gene *36b4*. Primer sequences are listed in Supplementary Table 2.

Adenoviral transduction

We constructed an scAAVrh.74.MHCK7.hESRRG transgene cassette using the *MHCK7* promoter to establish a skeletal muscle-specific *Esrrg* knockdown mouse model (DesignGene Biotechnology). The related sequences are listed in Supplementary Table 3. *Kdm2a*^{SKO} mice were randomly divided into control and experimental groups.

Viral efficacy in the muscle was achieved through intravenous injection into the tail vein of *Kdm2a*^{SKO} mice at a total dose of 1×10^{12} vector genomes (equivalent to 5×10^{13} vector genomes per kg for a 20 g mouse). *Kdm2a*^{fl/fl} and *Kdm2a*^{SKO} mice injected with the scAAVrh.74.MHCK7.GFP served as controls. The experiments were performed following 1 month of transduction.

Administration of Kdm2a inhibitor

The 8-week-old WT mice were fed a HFD for 16 weeks to induce obesity and insulin resistance. These mice were kept on HFD but subjected to a sustained cold challenge for 2 weeks, and daminozide was administered by intraperitoneal injection at $50 \text{ mg kg}^{-1} \text{ day}^{-1}$ or $100 \text{ mg kg}^{-1} \text{ day}^{-1}$ or the same volume of PBS, respectively, randomly throughout the cold challenge.

Seahorse assay

Basal oxygen consumption rate was measured using a Seahorse XFe24 analyzer (Agilent Technologies) according to the manufacturer's instructions. C2C12 myoblasts were differentiated in 24-well plates and stimulated with palmitic acid for 24 h at day 7 of differentiation. The differentiated cells were trypsinized and reseeded in the Seahorse XF24-microplates (50K cells per well) on day 8 of differentiation and assayed on day 9 of differentiation. Myotubes were switched to DMEM (no bicarbonate) with 5 mM glucose and 1 mM pyruvate 1 h before the assay. Respiration was measured three times followed by the injection of oligomycin (2 mM final), carbonyl cyanide 4-(trifluoromethoxy) phenylhydrazone (1 mM) and rotenone or antimycin A (1 mM), with three measurements after each injection. Data were normalized to protein content.

Mass spectrometry analysis of co-IP products

The collected C2C12 myotubes were washed three times with ice-cold PBS and then lysed in immunoprecipitation lysis buffer (Beyotime Biotechnology) containing 1% SDS, 1 mM phenylmethylsulfonyl fluoride and 10 mM *N*-ethylmaleimide (Sigma-Aldrich) in the presence of protease inhibitor cocktail ($10 \mu\text{g l}^{-1}$ aprotinin, $10 \mu\text{g l}^{-1}$ leupeptin, 5 mM sodium pyrophosphate and 1 mM Na_3VO_4). Immunoprecipitation was performed by incubating with an anti-H3K36me2 antibody overnight at 4 °C with rotation, followed by cross-linking to protein G (HY-K0202, MCE) for an additional 2 h at 4 °C. The resulting co-IP products were subjected to liquid chromatography coupled with tandem mass spectrometry analysis (PTM BioLabs). The potential candidates were determined by detecting more than two specific peptides. After washes with immunoprecipitation lysis buffer, the beads were eluted in Laemmli buffer and resolved by SDS-PAGE.

Immunoprecipitation assay

C2C12 myotubes were transfected with Mrg15-Flag plasmids for 48 h. Cell lysates were incubated with IgG or anti-Flag antibodies overnight at 4 °C. Lysates of Gas tissues were incubated with IgG or anti-H3K36me2 antibodies overnight at 4 °C. The next day, lysates were incubated with protein A/G magnetic beads (HY-K0202, MCE, USA) for 6 h and washed three times using lysis buffer. The levels of Flag and H3K36me2 or H3K36me2 and Mrg15 were then analysed by western blotting. Cell lysates of C2C12 myotubes were incubated with IgG or anti-H3K36me2 antibodies overnight at 4 °C.

ERthermAC analysis

C2C12 myoblasts were differentiated in 24-well plates as above. At day 7 of differentiation, myotubes were treated with ERthermAC (Emdmillipore SCT057) (250 nM) for 30 min, and the cells were washed three times with PBS and then subjected to flow cytometry analysis. The gating strategy is provided in Supplementary Fig. 4g.

Electron microscopy

Muscle slices were fixed in 2% formaldehyde and 2.5% glutaraldehyde in 0.1 M sodium cacodylate buffer (pH 7.4). The sections were subjected to

electron microscopy using a JEOL 1200EX transmission electron microscope equipped with an AMT 2k CCD camera. Mitochondrial analysis was performed on $\times 10,000$ cross-section (2 nm per pixel) micrographs from Gas muscle. Five mice were analysed for each study group.

RNA-seq and ChIP-seq

RNA-seq was performed on three animals per genotype per group. Gas tissue from HFD-fed *Kdm2a*^{fl/fl} and *Kdm2a*^{SKO} mice was isolated and mRNA was then extracted and subjected to deep RNA-seq analysis (BGI Genomics). The prepared mRNA libraries were sequenced on an Illumina HiSeq 2500, and HISAT2 (v.2.0.4) software (the Center for Computational Biology) was used to map cleaned reads to the mm10 reference genome. Fragments per kilobase of exon per million mapped fragments (FPKM) were calculated using Cuffnorm (v.2.2.1) software (University of Washington). The calculated genes with a normalized FPKM of >1.0 were considered to be expressed. Significantly differentially expressed genes were defined as $\log_2(\text{fold change}) \geq 0.5$ with a *P* value of ≤ 0.05 . Heatmaps were generated using the R package pheatmap.

ChIP-seq was also conducted on the above-isolated Gas tissues from three HFD-fed *Kdm2a*^{fl/fl} and *Kdm2a*^{SKO} mice, respectively. ChIP assays were carried out using a ChIP assay kit (Beyotime Biotechnology), using an antibody against H3K36me2; a rabbit IgG was used for the control. The purified DNA library was then sequenced on a NovaSeq 6000 sequencer (Illumina; model PE150) by SeqHealth. The established library was verified by agarose electrophoresis, quantified using Qubit (v.2.0) and sequenced on the Illumina HiSeq 2500 PE150. Raw sequencing data were first filtered by Trimmomatic (v.0.36), low-quality reads were discarded and the reads contaminated with adaptor sequences were trimmed. The clean reads were mapped to the reference genome of *Sus scrofa* from GCF_000003025.6 using STAR software (v.2.5.3a) with default parameters. The distribution, coverage, homogeneity and chain specificity of reads were next evaluated by RSeQC (v.2.6). Peaks in the ChIP-seq datasets were called with MACS2 (v.2.1.1) and the associated genes were identified using Homer (v.4.10). The distribution of call peak on the chromosomes and functional elements was performed by deep Tools (v.2.4.1) and ChIP seeker (v.1.5.1). Peak maps of reads across the genome were described using IGV (v.2.4.16). The motif analysis was performed using Homer (v.4.10). Gene Ontology analysis and KEGG enrichment analysis for the peak-related genes were both implemented by KOBAS software (v.2.1.1) with a corrected *P* value cutoff of 0.05.

Statistical analysis

All animals used in this study were randomly grouped. No statistical methods were used to predetermine sample sizes, but our sample sizes were similar to those reported in previous publications^{21,23,71,72}. All data are expressed as mean \pm s.e.m., and all in vitro studies were performed at least three independent times with replications unless otherwise stated. Data distribution was assumed to be normal, but this was not formally tested. Statistical analyses of the data were conducted with GraphPad Prism (v.5) software using unpaired two-tailed Student's *t*-tests, one-way ANOVA where appropriate, two-way ANOVA followed by Bonferroni's multiple comparisons test or two-sided Spearman's correlation. For all statistical comparisons, *P* values of <0.05 were considered statistically significant.

Reporting summary

Further information on research design is available in the Nature Portfolio Reporting Summary linked to this article.

Data availability

All data supporting the findings of this study are available within the article and/or its supplementary materials. The raw numbers for charts and graphs are available in the Source Data file whenever possible. The RNA-seq data (<https://www.ncbi.nlm.nih.gov/sra/PRJNA1163094>) and

ChIP-seq data (<https://www.ncbi.nlm.nih.gov/sra/PRJNA1165927>) have both been deposited in the NCBI public repository Sequence Read Archive. Source data are provided with this paper.

References

- Fujimaki, S. et al. The endothelial Dll4-muscular Notch2 axis regulates skeletal muscle mass. *Nat. Metab.* **4**, 180–189 (2022).
- Egan, B. & Zierath, J. R. Exercise metabolism and the molecular regulation of skeletal muscle adaptation. *Cell Metab.* **17**, 162–184 (2013).
- Meng, Z. X. et al. Baf60c drives glycolytic metabolism in the muscle and improves systemic glucose homeostasis through Deptor-mediated Akt activation. *Nat. Med.* **19**, 640–645 (2013).
- Jin, L. et al. The muscle-enriched myokine Musclin impairs beige fat thermogenesis and systemic energy homeostasis via Tfr1/PKA signaling in male mice. *Nat. Commun.* **14**, 4257 (2023).
- Severinsen, M. C. K. & Pedersen, B. K. Muscle-organ crosstalk: the emerging roles of myokines. *Endocr. Rev.* **41**, 594–609 (2020).
- Boström, P. et al. A PGC1- α -dependent myokine that drives brown-fat-like development of white fat and thermogenesis. *Nature* **481**, 463–468 (2012).
- Frampton, J., Murphy, K. G., Frost, G. & Chambers, E. S. Short-chain fatty acids as potential regulators of skeletal muscle metabolism and function. *Nat. Metab.* **2**, 840–848 (2020).
- Hargreaves, M. & Spriet, L. L. Skeletal muscle energy metabolism during exercise. *Nat. Metab.* **2**, 817–828 (2020).
- Fritzen, A. M., Lundsgaard, A.-M. & Kiens, B. Tuning fatty acid oxidation in skeletal muscle with dietary fat and exercise. *Nat. Rev. Endocrinol.* **16**, 683–696 (2020).
- Goodpaster, B. H., Theriault, R., Watkins, S. C. & Kelley, D. E. Intramuscular lipid content is increased in obesity and decreased by weight loss. *Metabolism* **49**, 467–472 (2000).
- Mengeste, A. M., Rustan, A. C. & Lund, J. Skeletal muscle energy metabolism in obesity. *Obesity (Silver Spring)* **29**, 1582–1595 (2021).
- Moriggi, M. et al. Skeletal muscle proteomic profile revealed gender-related metabolic responses in a diet-induced obesity animal model. *Int. J. Mol. Sci.* **22**, 4680 (2021).
- DeFronzo, R. A. & Tripathy, D. Skeletal muscle insulin resistance is the primary defect in type 2 diabetes. *Diabetes Care* **32**, S157–S163 (2009).
- Xu, J. et al. Myofiber Baf60c controls muscle regeneration by modulating Dkk3-mediated paracrine signaling. *J. Exp. Med.* **220**, e20221123 (2023).
- Gaster, M., Staehr, P., Beck-Nielsen, H., Schrøder, H. D. & Handberg, A. GLUT4 is reduced in slow muscle fibers of type 2 diabetic patients: Is insulin resistance in type 2 diabetes a slow, type 1 fiber disease? *Diabetes* **50**, 1324–1329 (2001).
- Stuart, C. A. et al. Slow-twitch fiber proportion in skeletal muscle correlates with insulin responsiveness. *J. Clin. Endocrinol. Metab.* **98**, 2027–2036 (2013).
- Kelley, D. E., He, J., Menshikova, E. V. & Ritov, V. B. Dysfunction of mitochondria in human skeletal muscle in type 2 diabetes. *Diabetes* **51**, 2944–2950 (2002).
- Howlett, K. F. & McGee, S. L. Epigenetic regulation of skeletal muscle metabolism. *Clin. Sci. (Lond.)* **130**, 1051–1063 (2016).
- van Dijk, S. J., Tellam, R. L., Morrison, J. L., Muhlhauser, B. S. & Molloy, P. L. Recent developments on the role of epigenetics in obesity and metabolic disease. *Clin. Epigenetics* **7**, 66 (2015).
- Long, Y., Mao, C., Liu, S., Tao, Y. & Xiao, D. Epigenetic modifications in obesity-associated diseases. *MedComm (2020)* **5**, e496 (2024).
- Chen, L. et al. *Kdm2a* deficiency in macrophages enhances thermogenesis to protect mice against HFD-induced obesity by enhancing H3K36me2 at the *Pparg* locus. *Cell Death Differ.* **28**, 1880–1899 (2021).
- Cheng, J. et al. Loss of Mbd2 protects mice against high-fat diet-induced obesity and insulin resistance by regulating the homeostasis of energy storage and expenditure. *Diabetes* **65**, 3384–3395 (2016).
- Xie, H. et al. SUMOylation of ERp44 enhances Ero1 α ER retention contributing to the pathogenesis of obesity and insulin resistance. *Metab. Clin. Exp.* **139**, 155351 (2023).
- Raichur, S. et al. Histone deacetylase 5 regulates glucose uptake and insulin action in muscle cells. *J. Mol. Endocrinol.* **49**, 203–211 (2012).
- Zhang, L. et al. Skeletal muscle-specific overexpression of PGC-1 α induces fiber-type conversion through enhanced mitochondrial respiration and fatty acid oxidation in mice and pigs. *Int. J. Biol. Sci.* **13**, 1152–1162 (2017).
- Kim, A. et al. Ablation of USP21 in skeletal muscle promotes oxidative fibre phenotype, inhibiting obesity and type 2 diabetes. *J. Cachexia Sarcopenia Muscle* **12**, 1669–1689 (2021).
- Song, M.-Y. et al. Sirt6 reprograms myofibers to oxidative type through CREB-dependent Sox6 suppression. *Nat. Commun.* **13**, 1808 (2022).
- Lin, J. et al. Transcriptional co-activator PGC-1 alpha drives the formation of slow-twitch muscle fibres. *Nature* **418**, 797–801 (2002).
- Meizoso-Huesca, A., Pearce, L., Barclay, C. J. & Launikonis, B. S. Ca²⁺ leak through ryanodine receptor 1 regulates thermogenesis in resting skeletal muscle. *Proc. Natl Acad. Sci. USA* **119**, e2119203119 (2022).
- Nomura, T. et al. Effects of long-term cold exposure on contractile muscles of rats. *Jpn J. Physiol.* **52**, 85–93 (2002).
- Suzuki, J., Gao, M., Ohinata, H., Kuroshima, A. & Koyama, T. Chronic cold exposure stimulates microvascular remodeling preferentially in oxidative muscles in rats. *Jpn J. Physiol.* **47**, 513–520 (1997).
- Bruton, J. D. et al. Increased fatigue resistance linked to Ca²⁺-stimulated mitochondrial biogenesis in muscle fibres of cold-acclimated mice. *J. Physiol.* **588**, 4275–4288 (2010).
- Chen, W. et al. Cold exposure alters lipid metabolism of skeletal muscle through HIF-1 α -induced mitophagy. *BMC Biol.* **21**, 27 (2023).
- Oberbach, A. et al. Altered fiber distribution and fiber-specific glycolytic and oxidative enzyme activity in skeletal muscle of patients with type 2 diabetes. *Diabetes Care* **29**, 895–900 (2006).
- Wan, F. et al. Mesenchymal stem cells inhibits migration and vasculogenic mimicry in nasopharyngeal carcinoma via exosomal MiR-125a. *Front. Oncol.* **12**, 781979 (2022).
- Axelrod, C. L. et al. Lipids activate skeletal muscle mitochondrial fission and quality control networks to induce insulin resistance in humans. *Metabolism* **121**, 154803 (2021).
- Wang, D. et al. GDF15 promotes weight loss by enhancing energy expenditure in muscle. *Nature* **619**, 143–150 (2023).
- Wang, X. et al. CircRNA-CREIT inhibits stress granule assembly and overcomes doxorubicin resistance in TNBC by destabilizing PKR. *J. Hematol. Oncol.* **15**, 122 (2022).
- Kriszt, R. et al. Optical visualisation of thermogenesis in stimulated single-cell brown adipocytes. *Sci. Rep.* **7**, 1383 (2017).
- Misra, J., Kim, D. K. & Choi, H. S. ERR γ : a junior orphan with a senior role in metabolism. *Trends Endocrinol. Metab.* **28**, 261–272 (2017).
- Sopariwala, D. H., Rios, A. S., Saley, A., Kumar, A. & Narkar, V. A. Estrogen-related receptor gamma gene therapy promotes therapeutic angiogenesis and muscle recovery in preclinical model of PAD. *J. Am. Heart Assoc.* **12**, e028880 (2023).
- Rangwala, S. M. et al. Estrogen-related receptor gamma is a key regulator of muscle mitochondrial activity and oxidative capacity. *J. Biol. Chem.* **285**, 22619–22629 (2010).

43. Leung, C. S. et al. H3K36 methylation and the chromodomain protein Eaf3 are required for proper cotranscriptional spliceosome assembly. *Cell Rep.* **27**, 3760–3769.e4 (2019).
44. Iwamori, N. et al. MRG15 is required for pre-mRNA splicing and spermatogenesis. *Proc. Natl Acad. Sci. USA* **113**, E5408–E5415 (2016).
45. Palmer, B. F. & Clegg, D. J. Metabolic flexibility and its impact on health outcomes. *Mayo Clin. Proc.* **97**, 761–776 (2022).
46. Park, G. et al. Quantitative analysis of metabolic fluxes in brown fat and skeletal muscle during thermogenesis. *Nat. Metab.* **5**, 1204–1220 (2023).
47. Damer, A. et al. Association of muscle fiber type with measures of obesity: a systematic review. *Obes. Rev.* **23**, e13444 (2022).
48. Lefort, N. et al. Increased reactive oxygen species production and lower abundance of complex I subunits and carnitine palmitoyltransferase 1B protein despite normal mitochondrial respiration in insulin-resistant human skeletal muscle. *Diabetes* **59**, 2444–2452 (2010).
49. Holloway, G. P., Bonen, A. & Spriet, L. L. Regulation of skeletal muscle mitochondrial fatty acid metabolism in lean and obese individuals. *Am. J. Clin. Nutr.* **89**, 455S–462S (2009).
50. Jacob, S. et al. Association of increased intramyocellular lipid content with insulin resistance in lean nondiabetic offspring of type 2 diabetic subjects. *Diabetes* **48**, 1113–1119 (1999).
51. Holloszy, J. O. Biochemical adaptations in muscle. Effects of exercise on mitochondrial oxygen uptake and respiratory enzyme activity in skeletal muscle. *J. Biol. Chem.* **242**, 2278–2282 (1967).
52. Richter, E. A. & Hargreaves, M. Exercise, GLUT4, and skeletal muscle glucose uptake. *Physiol. Rev.* **93**, 993–1017 (2013).
53. Evans, P. L., McMillin, S. L., Weyrauch, L. A. & Witczak, C. A. Regulation of skeletal muscle glucose transport and glucose metabolism by exercise training. *Nutrients* **11**, 2432 (2019).
54. Muscella, A., Stefàno, E., Lunetti, P., Capobianco, L. & Marsigliante, S. The regulation of fat metabolism during aerobic exercise. *Biomolecules* **10**, 1699 (2020).
55. Turner, N. et al. Excess lipid availability increases mitochondrial fatty acid oxidative capacity in muscle: evidence against a role for reduced fatty acid oxidation in lipid-induced insulin resistance in rodents. *Diabetes* **56**, 2085–2092 (2007).
56. Schakman, O., Kalista, S., Barbé, C., Loumaye, A. & Thissen, J. P. Glucocorticoid-induced skeletal muscle atrophy. *Int. J. Biochem. Cell Biol.* **45**, 2163–2172 (2013).
57. Dolan, E., Artioli, G. G., Pereira, R. M. R. & Gualano, B. Muscular atrophy and sarcopenia in the elderly: Is there a role for creatine supplementation? *Biomolecules* **9**, 642 (2019).
58. Allen, S. L. et al. Sarcopenia in chronic liver disease: mechanisms and countermeasures. *Am. J. Physiol. Gastrointest. Liver Physiol.* **320**, G241–g257 (2021).
59. Wang, X. et al. Metabolic inflexibility promotes mitochondrial health during liver regeneration. *Science* **384**, eadj4301 (2024).
60. Widmann, M., Nieß, A. M. & Munz, B. Physical exercise and epigenetic modifications in skeletal muscle. *Sports Med.* **49**, 509–523 (2019).
61. McGee, S. L. & Hargreaves, M. Histone modifications and exercise adaptations. *J. Appl. Physiol.* (1985) **110**, 258–263 (2011).
62. Potthoff, M. J. et al. Histone deacetylase degradation and MEF2 activation promote the formation of slow-twitch myofibers. *J. Clin. Invest.* **117**, 2459–2467 (2007).
63. Strahl, B. D. & Allis, C. D. The language of covalent histone modifications. *Nature* **403**, 41–45 (2000).
64. Shilatifard, A. Chromatin modifications by methylation and ubiquitination: implications in the regulation of gene expression. *Annu. Rev. Biochem.* **75**, 243–269 (2006).
65. Song, L. & Luo, Z. Q. Post-translational regulation of ubiquitin signaling. *J. Cell Biol.* **218**, 1776–1786 (2019).
66. Stillman, B. Histone modifications: insights into their influence on gene expression. *Cell* **175**, 6–9 (2018).
67. Barash, Y. et al. Deciphering the splicing code. *Nature* **465**, 53–59 (2010).
68. Ambrosini, S. et al. Methylation of the Hippo effector YAP by the methyltransferase SETD7 drives myocardial ischaemic injury: a translational study. *Cardiovasc. Res.* **118**, 3374–3385 (2023).
69. Zhu, X. et al. IRF4 in skeletal muscle regulates exercise capacity via PTG/glycogen pathway. *Adv. Sci. (Weinh.)* **7**, 2001502 (2020).
70. Zhang, J. et al. Myo9b mutations are associated with altered dendritic cell functions and increased susceptibility to autoimmune diabetes onset. *Nat. Commun.* **14**, 5977 (2023).
71. Huang, T. et al. Adipocyte-derived kynurenine promotes obesity and insulin resistance by activating the AhR/STAT3/IL-6 signaling. *Nat. Commun.* **13**, 3489 (2022).
72. Wang, Y. et al. MBD2 serves as a viable target against pulmonary fibrosis by inhibiting macrophage M2 program. *Sci. Adv.* **7**, eabb6075 (2021).

Acknowledgements

We are grateful to those patients who donated their skeletal muscles for the studies. We thank W. Mo and S. Liu from the Center of Biomedical Research, Tongji Hospital, Tongji Medical College, Huazhong University of Science and Technology for their help in animal studies. This study was supported by funding from the National Key R&D Program of China (2022YFA0806101 to C.-Y.W.); National Natural Science Foundation of China (91749207, 82130023 and 81920108009 to C.-Y.W., 82070808 to S.Z. and 82270885 to Q.L.Y.); Key Laboratory of Endocrine and Metabolic Diseases of Shanxi Province (202104010910009 to S.-W.L.); Fundamental Research Funds for the Central Universities, HUST (2021yjsCXCY097 to Y.-H.W.); Integrated Innovative Team for Major Human Diseases Program of Tongji Medical College, Huazhong University of Science and Technology (C.-Y.W.); and the Innovative Funding for Translational Research from Tongji Hospital (C.-Y.W.).

Author contributions

Y.-H.W., H.X., Q.-R.L. and N.W. contributed equally to this work. Y.-H.W. and H.X. designed the experiments and analysed the data. Y.-H.W. and H.X. wrote the manuscript. Xi L. and F.S. were actively involved in the experimental design and wrote the initial version of the manuscript. Y.-H.W., H.X., Q.-R.L. and N.W. performed the majority of the experiments. Y.-H.W., Q.-R.L., N.W., R.-H.D. J.G. and T.H. performed the RT-qPCR and western blot. Y.-H.W. and J.-H.Z. assisted in the construction of *Kdm2a*-KO cells. Y.-H.W., J.G., Z.-C.G., Xin L., Q.-L.Y., Y.L. and T.H. helped with the animal experiments. Y.-H.W., Y.W., H.Y., S.-W.L. and S.Z. contributed to the study of the intron shear mechanism. Y.-H.W., Xi L., D.-N.S. and T.W. performed the Seahorse experiments. Y.-H.W. and W.K. collected clinical samples. H.Y., W.K., S.Z. and C.-Y.W. assisted with study design and discussion of manuscript preparation. C.-Y.W. wrote and edited the manuscript and is responsible for the integrity of the data.

Competing interests

The authors declare no competing interests.

Additional information

Extended data is available for this paper at <https://doi.org/10.1038/s42255-024-01210-9>.

Supplementary information The online version contains supplementary material available at <https://doi.org/10.1038/s42255-024-01210-9>.

Correspondence and requests for materials should be addressed to Shu Zhang, Hao Yin, Wen Kong or Cong-Yi Wang.

Peer review information *Nature Metabolism* thanks F. Jeffrey Dilworth, Xingxing Kong and Zhuo-Xian Meng for their contribution to the peer review of this work. Primary Handling Editors: Jean Nakhle and Ashley Castellanos-Jankiewicz, in collaboration with the *Nature Metabolism* team.

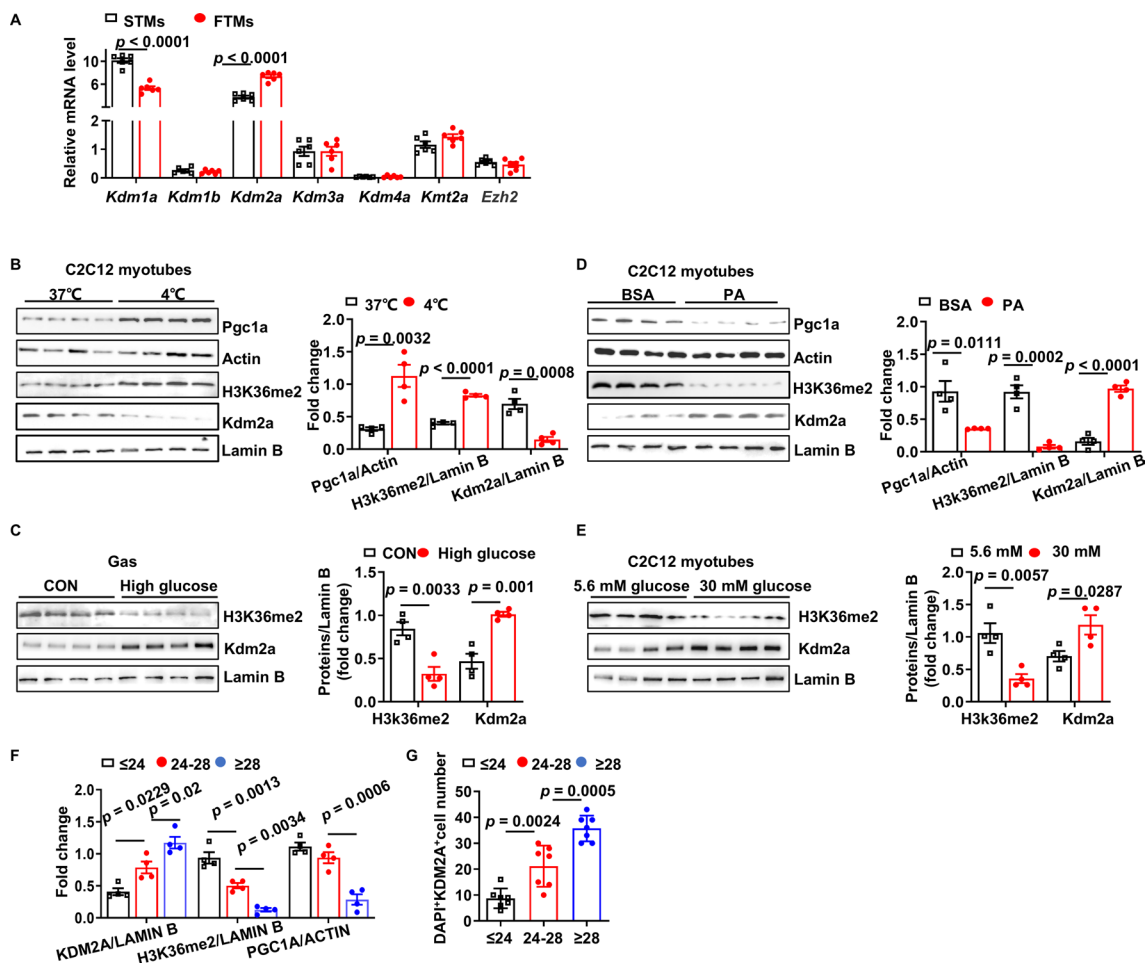
Reprints and permissions information is available at www.nature.com/reprints.

Publisher's note Springer Nature remains neutral with regard to jurisdictional claims in published maps and institutional affiliations.

Open Access This article is licensed under a Creative Commons Attribution-NonCommercial-NoDerivatives 4.0 International License,

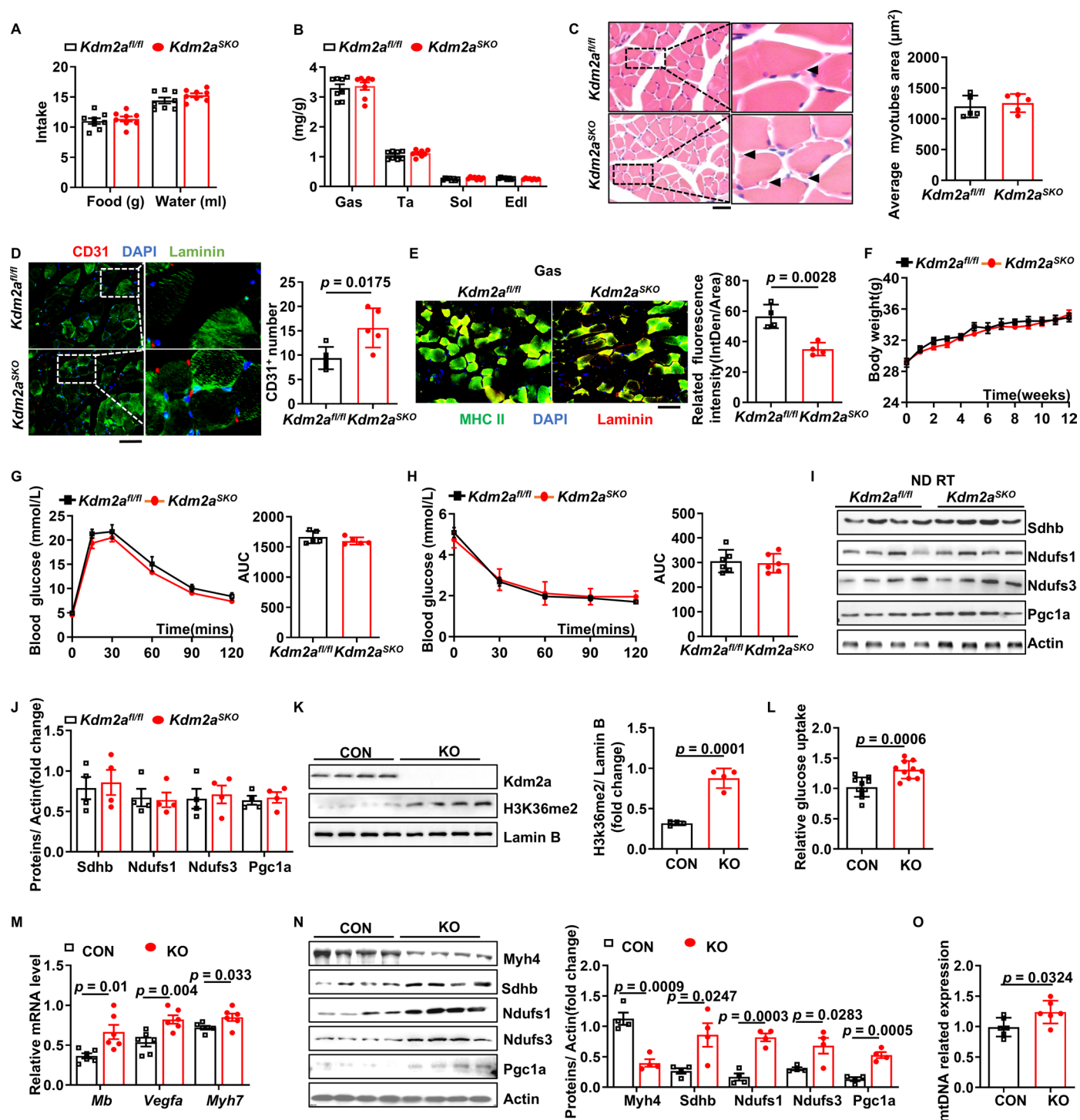
which permits any non-commercial use, sharing, distribution and reproduction in any medium or format, as long as you give appropriate credit to the original author(s) and the source, provide a link to the Creative Commons licence, and indicate if you modified the licensed material. You do not have permission under this licence to share adapted material derived from this article or parts of it. The images or other third party material in this article are included in the article's Creative Commons licence, unless indicated otherwise in a credit line to the material. If material is not included in the article's Creative Commons licence and your intended use is not permitted by statutory regulation or exceeds the permitted use, you will need to obtain permission directly from the copyright holder. To view a copy of this licence, visit <http://creativecommons.org/licenses/by-nc-nd/4.0/>.

© The Author(s) 2025



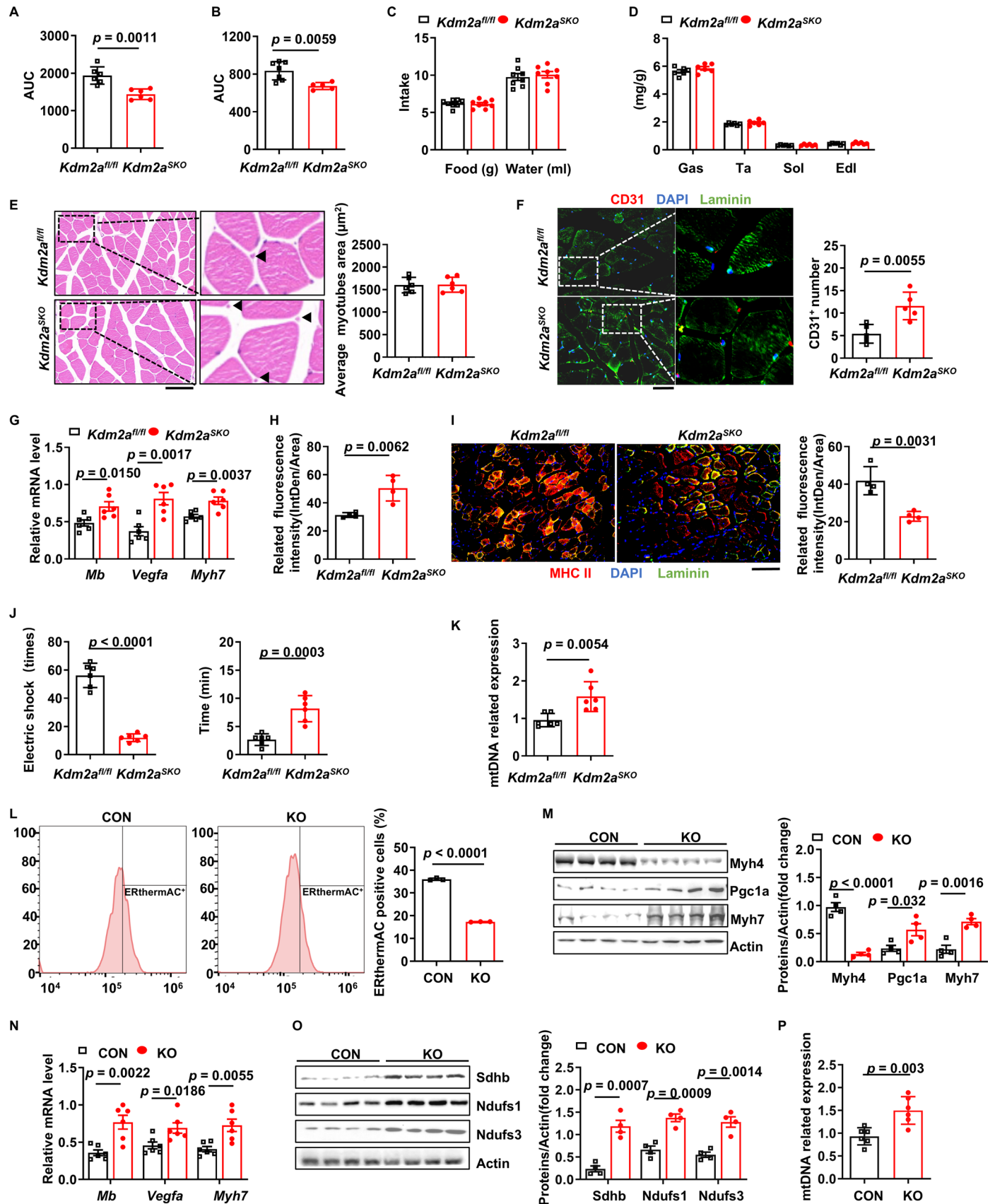
Extended Data Fig. 1 | Kdm2a catalyzes H3K36me2 demethylation and reduces STM proportion. (a) Relative mRNA expression of *Kdm1a*, *Kdm1b*, *Kdm2a*, *Kdm3a*, *Kdm4a*, *Kmt2a* and *Ezh2* between STMs (Sol) and FTMs (Edl) from WT male mice fed with ND ($n = 6$ per group). (b) Western blot analysis of Pgc1a, Kdm2a and H3K36me2 in C2C12 myotubes under 37°C and 4°C treatment ($n = 4$ per group). Protein quantitative analysis (right). (c) Western blot analysis of the expression of Kdm2a and H3K36me2 in hyperglycemic male mice Gas tissues ($n = 4$ per group). Protein quantitative analysis (right). (d) Western blot analysis

of Pgc1a, Kdm2a and H3K36me2 in C2C12 myotubes after PA stimulation for 48h ($n = 4$ per group). Protein quantitative analysis (right). (e) Western blot analysis of the expression of Kdm2a and H3K36me2 in C2C12 myotubes after 30 mM glucose stimulation for 24h ($n = 4$ per group). Protein quantitative analysis (right). (f) Protein quantitative analysis of Fig. 1h. (g) DAPI+KDM2A+ cell number of Fig. 1i. Data were expressed as mean \pm SEM. Statistical significance was assessed by two-sided Student's *t* test (a-g).



Extended Data Fig. 2 | Enhanced glucose consumption in *Kdm2a* KO mice under cold insult. (a) The food and water intake during metabolic cages monitoring of cold-adapted *Kdm2a^{fl/fl}* and *Kdm2a^{SKO}* mice ($n = 8$ per group). (b) Muscle mass analysis between ND *Kdm2a^{fl/fl}* and *Kdm2a^{SKO}* mice with cold challenge ($n = 8$ per group). (c) Representative H&E staining images in slices of cold-adapted *Kdm2a^{fl/fl}* and *Kdm2a^{SKO}* mice Gas tissues, average myotubes area analysis, Arrows indicated the blood vessels, Scale bars, 50 μm , ($n = 5$ per group). (d) Representative immunostaining of Laminin (green), CD31 (red) and DAPI (blue) in Gas tissue cross sections of cold-adapted *Kdm2a^{fl/fl}* and *Kdm2a^{SKO}* male mice, CD31⁺ number analysis (right), Scale bars, 50 μm , ($n = 5$ per group). (e) Representative immunostaining of Laminin (red), MHC II (green) and DAPI (blue) in Gas tissue cross sections of cold-adapted *Kdm2a^{fl/fl}* and *Kdm2a^{SKO}* male mice. Scale bars, 50 μm , ($n = 4$ per group). (f) Body weight gain of *Kdm2a^{fl/fl}* and *Kdm2a^{SKO}* mice fed with ND without cold challenge ($n = 5$ per group). (g) ITT

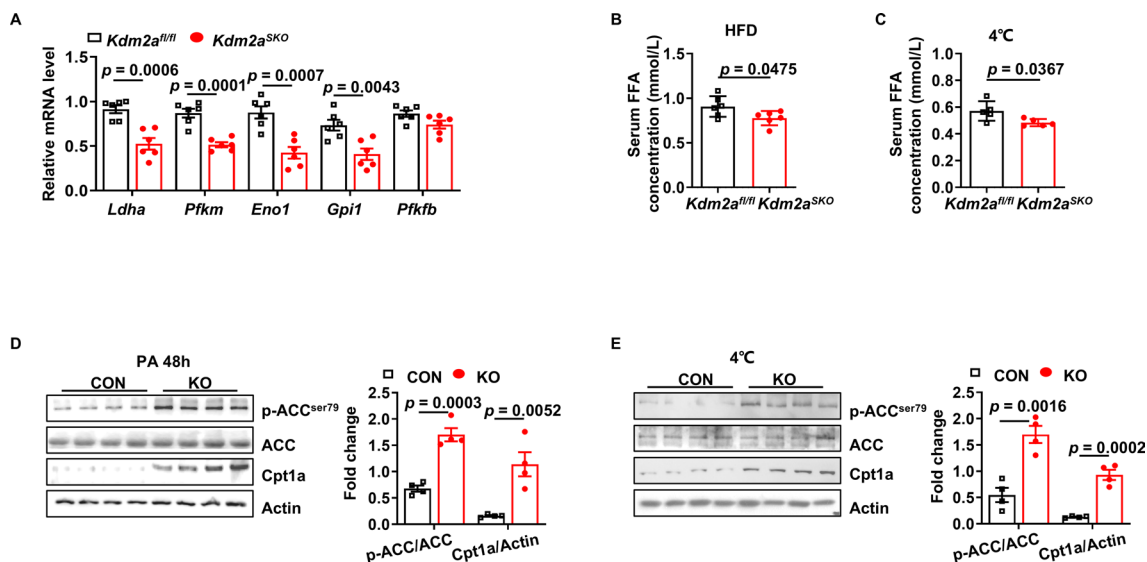
and (h) ITT of *Kdm2a^{fl/fl}* and *Kdm2a^{SKO}* mice fed with ND without cold challenge ($n = 4/5$ per group). AUC analysis (right). (i) Western blot analyses Sdhb, Ndufs1, Ndufs3 and Pgc1a of ND *Kdm2a^{fl/fl}* and *Kdm2a^{SKO}* mice without cold challenge ($n = 4$ per group). Protein quantitative analysis (j). (k) Western blot analysis of H3K36me2 and Kdm2a in *Kdm2a*-WT and *Kdm2a*-KO C2C12 myotubes ($n = 4$ per group). Protein quantitative analysis (right). (l-o) Treat *Kdm2a*-WT and *Kdm2a*-KO C2C12 myotubes with 2 hours of cold stimulation. (l) Glucose uptake assay in *Kdm2a*-WT and *Kdm2a*-KO C2C12 myotubes with cold stimulation ($n = 10$). (m) RT-qPCR analysis of *Mb*, *Vegfa* and *Myh7* expression ($n = 6$ per group). (n) Western blot analysis of Myh4, Sdhb, Ndufs1, Ndufs3, Pgc1a ($n = 4$ per group). Protein quantitative analysis (right). (o) mtDNA copy number analysis ($n = 6$ per group). Data were expressed as mean \pm SEM. Statistical significance was assessed by two-way ANOVA (f-h) followed with Bonferroni's multiple comparisons test or two-sided Student's *t* test (a-e, i-o).



Extended Data Fig. 3 | See next page for caption.

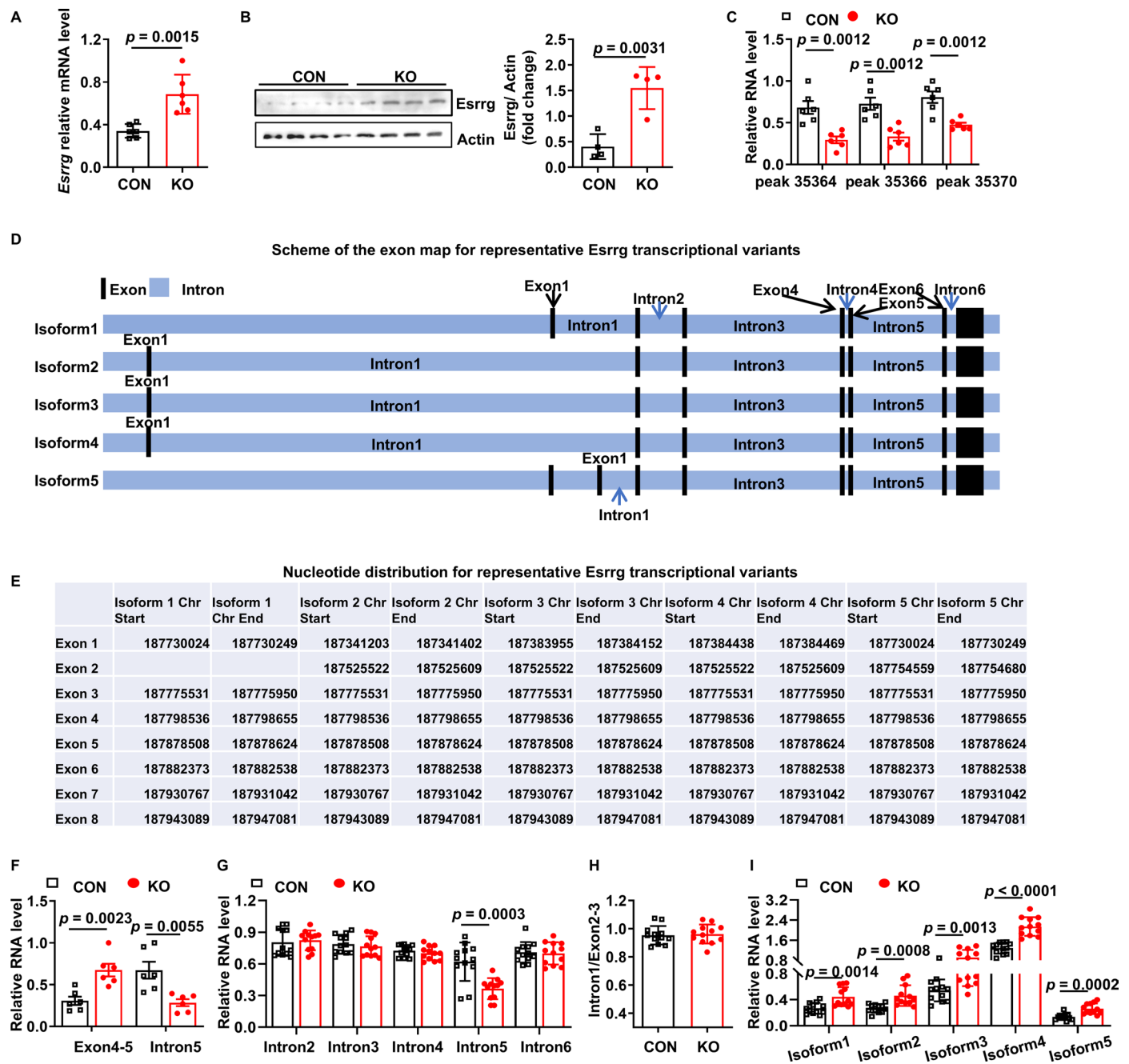
Extended Data Fig. 3 | Loss of *Kdm2a* promotes lipid consumption in HFD induced mice. (a) The quantitative analysis of Fig. 3f and (b) Fig. 3g. (c) Food and water intake monitoring of metabolic experiments ($n = 8$ per group). (d) Muscle mass analysis of *Kdm2a*^{fl/fl} and *Kdm2a*^{SKO} male mice on 16-week HFD ($n = 6$ per group). (e) Representative H&E staining images in Gas tissue cross sections of HFD-fed *Kdm2a*^{fl/fl} and *Kdm2a*^{SKO} male mice, average myotubes area analysis (right), Arrows indicated the blood vessels, Scale bars, 100 μm , ($n = 6$ per group). (f) Representative immunostaining of Laminin (green), CD31 (red) and DAPI (blue) in Gas tissue cross sections of HFD-fed *Kdm2a*^{fl/fl} and *Kdm2a*^{SKO} male mice, CD31⁺ number analysis (right), Scale bars, 50 μm , ($n = 5$ per group). (g) RT-qPCR analysis of *Mb*, *Vegfa* and *Myh7* expression in HFD-fed *Kdm2a*^{fl/fl} and *Kdm2a*^{SKO} male mice ($n = 6$ per group). (h) Related fluorescence intensity analysis of Fig. 3p ($n = 4$ per group). (i) Representative immunostaining of Laminin

(green), MHC II (red) and DAPI (blue) in Ta tissue cross sections of HFD-fed *Kdm2a*^{fl/fl} and *Kdm2a*^{SKO} male mice. Scale bars, 100 μm , ($n = 4$ per group). (j) Treadmill endurance monitoring, electric shock times (left) ($n = 6$ per group) and exhaustion time (right) of HFD-fed *Kdm2a*^{fl/fl} and *Kdm2a*^{SKO} male mice ($n = 6$ per group). (k) The mtDNA copy number analysis of HFD-fed *Kdm2a*^{fl/fl} and *Kdm2a*^{SKO} male mice ($n = 6$ per group). (l-p) *Kdm2a*-WT and *Kdm2a*-KO C2C12 myotubes were stimulated with PA for 48h, and then (l) Flow cytometry analysis of the thermosensitive fluorescent dye stained ERthermAC-positive cells ($n = 3$ per group), western blot analysis of Pgc1, Myh4, Myh7 (m), Sdhb, Ndufs1, Ndufs3 (o) ($n = 4$ per group). Protein quantitative analysis (right). (n) RT-qPCR analysis of *Mb*, *Vegfa* and *Myh7* expression ($n = 6$ per group). (p) Relative mtDNA copy number analysis ($n = 6$ per group). Data were expressed as mean \pm SEM. Two-sided unpaired student's *t*-test was used for statistical analysis (a-p).



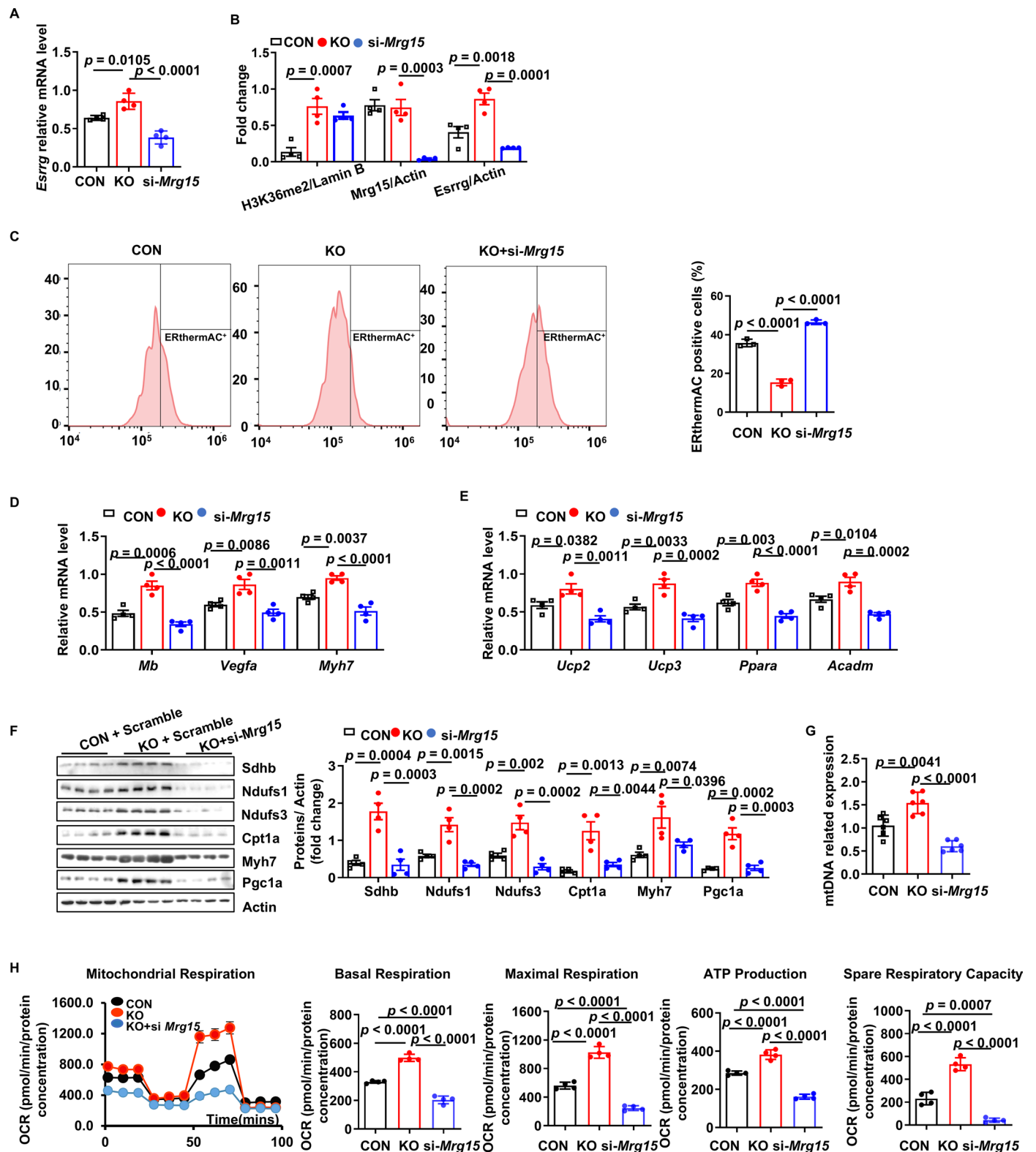
Extended Data Fig. 4 | *Kdm2a* remodels lipid metabolism under HFD challenge. (a) RT-qPCR analysis of glycolytic related gene expression in HFD-fed *Kdm2a^{fl/fl}* and *Kdm2a^{SKO}* male mice ($n = 6$ per group). (b) FFA levels in HFD-fed *Kdm2a^{fl/fl}* and *Kdm2a^{SKO}* male mice serum ($n = 6$ per group). (c) FFA levels in cold-adapted *Kdm2a^{fl/fl}* and *Kdm2a^{SKO}* male mice serum ($n = 6$ per group). (d) Western blot analysis of p-ACC/ACC and Cpt1a levels in *Kdm2a*-WT and *Kdm2a*-KO

myotubes after PA stimulation ($n = 4$ per group). Protein quantitative analysis (right). (e) Western blot analysis of p-ACC/ACC and Cpt1a levels in *Kdm2a*-WT and *Kdm2a*-KO myotubes after 4°C stimulation ($n = 4$ per group). Protein quantitative analysis (right). Data were expressed as mean \pm SEM. Student's *t*-test was used for statistical analysis (a-e).



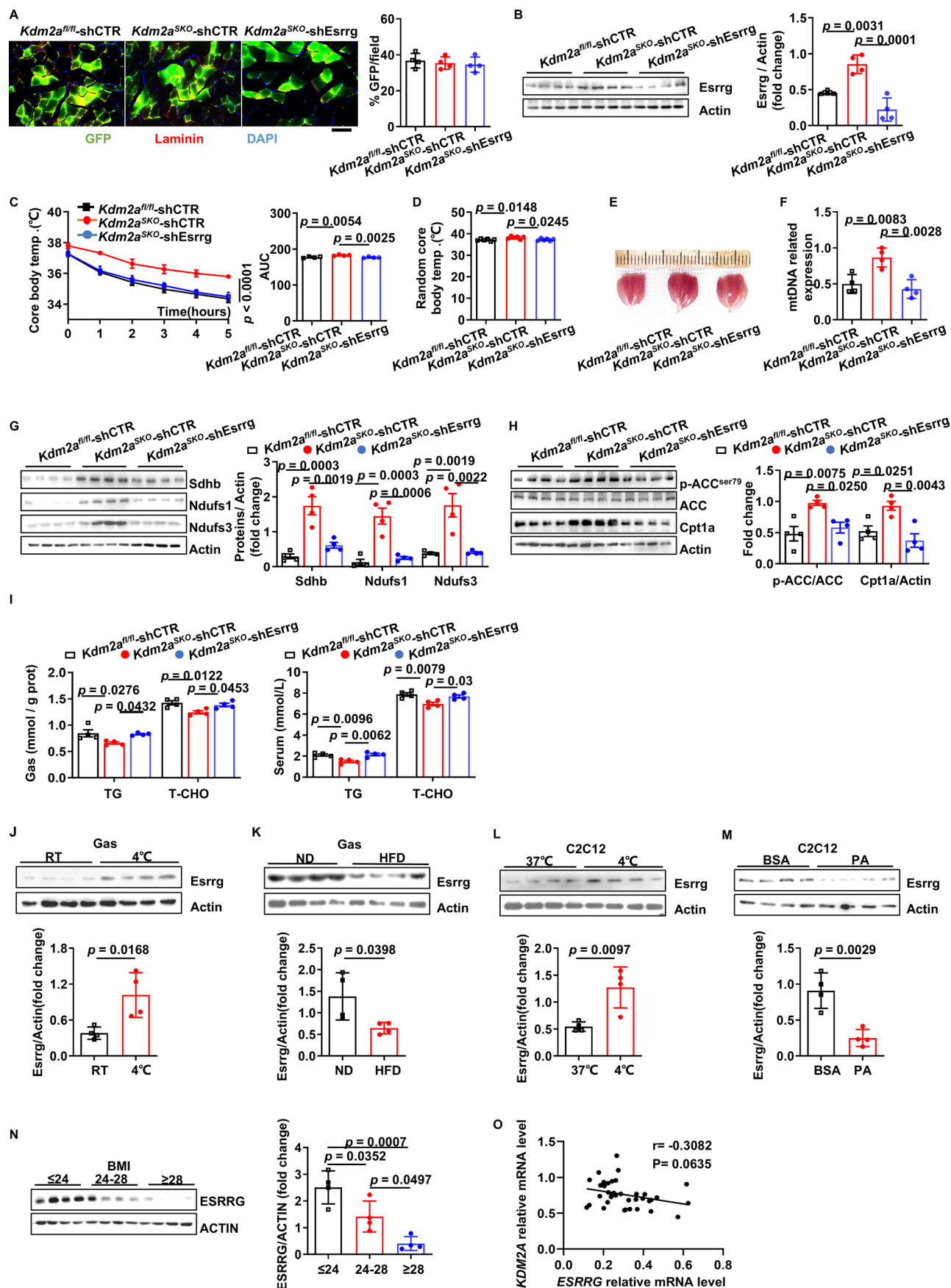
Extended Data Fig. 5 | *Esrrg* pre-mRNA splicing reshapes muscle metabolic pattern. (a) RT-qPCR and (b) Western blot analysis of *Esrrg* in *Kdm2a*-WT and *Kdm2a*-KO C2C12 myotubes after PA stimulation ($n=4/6$ per group). Protein quantitative analysis (right). (c) RT-qPCR analysis of transcribed intron fragments (peak 35364, peak 35366, peak 35370) in *Kdm2a*-WT and *Kdm2a*-KO C2C12 myotubes with PA stimulation ($n=6$ per group). (d) Scheme of the exon map for representative *Esrrg* transcriptional variants (Relative to NC_000066.7 version). (e) Nucleotide distribution for representative *Esrrg* transcriptional variants (Relative to NC_000066.7 version). (f) Relative RNA level analysis of transcribed exon4-5 and Intron5 fragments in *Kdm2a*-WT and *Kdm2a*-KO C2C12

myotubes after PA stimulation ($n=6$ per group). (g) Relative RNA level analysis of transcribed Intron2, Intron3, Intron4, Intron5 and Intron6 between *Kdm2a*-WT and *Kdm2a*-KO C2C12 myotubes after PA stimulation ($n=6$ per group). (h) The ratio of the relative transcription of the variable shear region (Intron1) to the adjacent exon region (Exon2-3) in *Kdm2a*-WT and *Kdm2a*-KO C2C12 myotubes with PA stimulation ($n=6$ per group). (i) Analysis of relative abundance of different *Esrrg* isoforms in *Kdm2a*-WT and *Kdm2a*-KO C2C12 myotubes with PA stimulation ($n=6$ per group). Data were expressed as mean \pm SEM. Two-sided unpaired student's *t*-test was used for statistical analysis (a-c, f-i).



Extended Data Fig. 6 | *Esrrg* pre-mRNA splicing reshapes muscle metabolic pattern. (a-h) After transfection of si-*Mrg15*, myotubes were treated by PA for 48 hours. (a) RT-qPCR analysis of *Esrrg* expression levels in *Kdm2a*-WT myotubes, *Kdm2a*-KO myotubes and *Kdm2a*-KO+si-*Mrg15* myotubes ($n = 4$ per group). (b) Quantitative analysis of Fig. 5m was performed ($n = 4$ per group). (c) Flow cytometry analysis of the thermosensitive fluorescent dye stained ERtherm AC-positive cells ($n = 3$ per group), along with the quantitative analysis (right). (d) RT-qPCR analysis of *Mb*, *Vegfa* and *Myh7* expression ($n = 4$ per group), (e) RT-qPCR analysis of *Ucp2*, *Ucp3*, *Ppara* and *Acadm* expression ($n = 4$ per group), (f) western

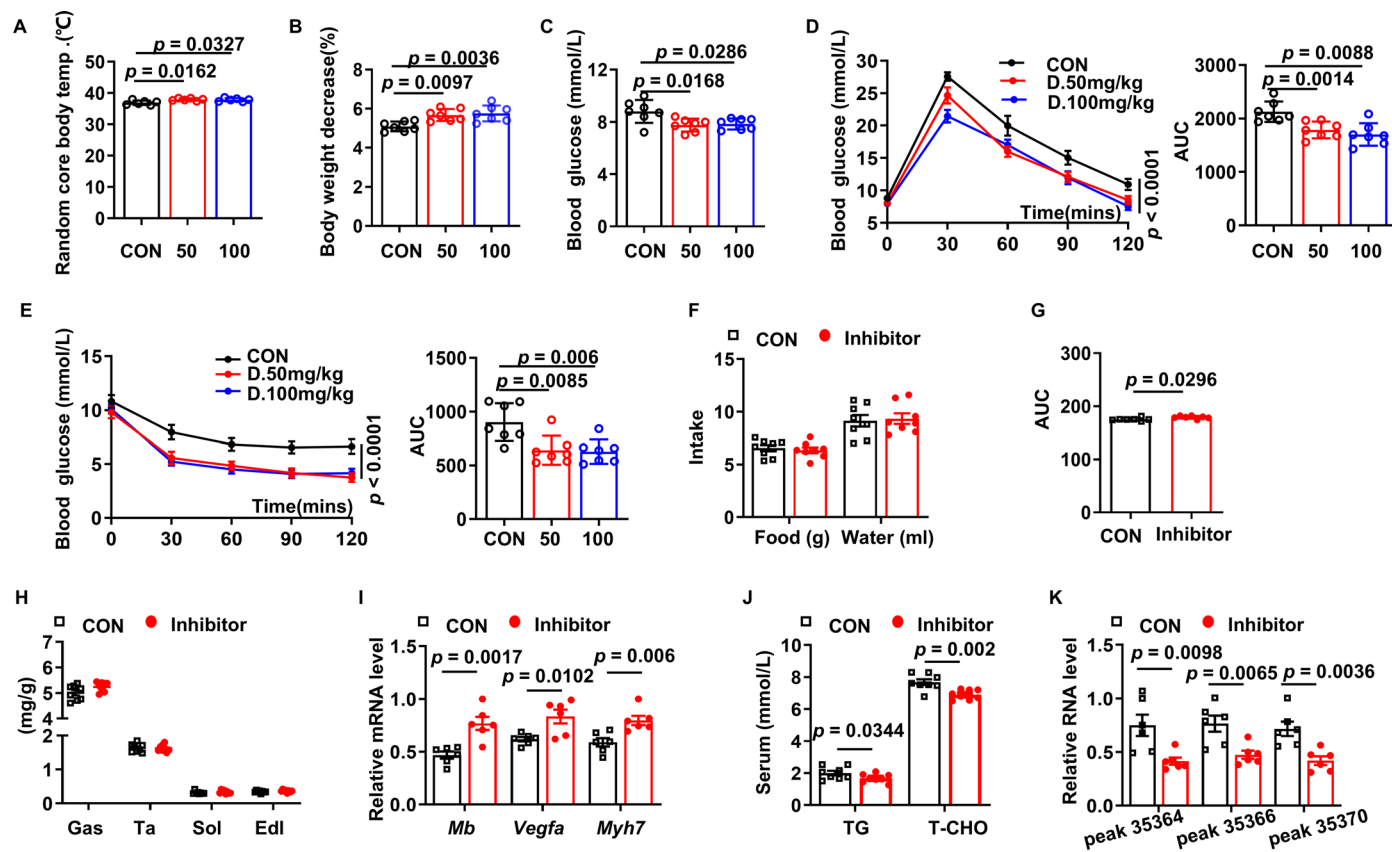
blot analysis of Sdhb, Ndufs1, Ndufs3, Cpt1a, Myh7 and Pgc1a expression ($n = 4$ per group), the quantitative analysis (right). (g) Relative mtDNA copy number analysis ($n = 6$ per group). (h) OCR of *Kdm2a*-WT myotubes, *Kdm2a*-KO myotubes and *Kdm2a*-KO+si-*Mrg15* myotubes following 48h of PA stimulation, which was assessed before and after sequential treatment with oligomycin, FCCP, rotenone, and antimycin A. The mitochondrial respiration rates of basal and maximal respiration, ATP production and spare respiratory capacity were shown ($n = 4$ per group). Data were expressed as mean \pm SEM. Two-sided unpaired student's *t*-test was used for statistical analysis.



Extended Data Fig. 7 | See next page for caption.

Extended Data Fig. 7 | *Esrrg* pre-mRNA splicing reshapes muscle metabolic pattern. (a-i) Using the scAAVrh.74.MHCK7.Hesrrg particles (defined as *Kdm2a*^{SKO}-shEsrrg mice), skeletal muscle-specific *Esrrg* knockdown model was generated. Injection of male mice with scAAVs carrying shCTR was used as controls (defined as *Kdm2a*^{fl/fl}-shCTR, *Kdm2a*^{SKO}-shCTR). In *Kdm2a*^{fl/fl}-shCTR, *Kdm2a*^{SKO}-shCTR and *Kdm2a*^{SKO}-shEsrrg mice, (a) the representative staining of Ta myofibers one month post-administration. Quantification of GFP⁺ myofibers (right) ($n = 4$ per group). GFP (green), Laminin (red) and DAPI (blue). Scale bars: 50 μm . (b) Western blot analysis of *Esrrg* and *Pgc1a* ($n = 4$ per group). Protein quantitative analysis (right). (c) The core body temperature monitoring under 4°C ($n = 6$ per group). (d) The random core body temperature at RT ($n = 6$ per group). (e) Representative image of Gas tissues ($n = 4$ per group). (f) mtDNA copy number analysis ($n = 6$ per group). (g) Western blot analysis of *Sdhb*, *Ndufs1*, *Ndufs3* ($n = 4$ per group). Protein quantitative analysis (right). (h) Western blot analysis of p-ACC/ACC and *Cpt1a* levels ($n = 4$ per group). Protein quantitative

analysis (right). (i) TG and T-CHO levels in Gas (left) or serum (right) ($n = 4$ per group). (j) Western blot analysis of *Esrrg* in WT mice Gas between RT and 4°C ($n = 4$ per group). Protein quantitative analysis (below). (k) Western blot analysis of *Esrrg* in WT mice Gas between ND and HFD ($n = 4$ per group). Protein quantitative analysis (below). (l) Western blot analysis of *Esrrg* in C2C12 myotubes between 37°C and 4°C ($n = 4$ per group). Protein quantitative analysis (below). (m) Western blot analysis of *Esrrg* in C2C12 myotubes after PA stimulation ($n = 4$ per group). Protein quantitative analysis (below). (n) Western blot analysis of *ESRRG* expression in BMI \leq 24 group, 24 < BMI < 28 group and patients with BMI \geq 28 group, ($n = 3$ per group). Protein quantitative analysis (right). (o) *KDM2A* and *ESRRG* correlation analysis in human Ta tissues ($n = 37$). Data were expressed as mean \pm SEM. Statistical significance was assessed by one-way ANOVA (a), two-way ANOVA (c) followed with Bonferroni's multiple comparisons test, two-sided Student's *t*-test (b, d, f-n) or two-sided Spearman's correlation (o).



Extended Data Fig. 8 | Kdm2a could be a viable target against metabolic stress. (a-e) After 16w HFD, WT male mice were injected with PBS (5% DMSO) or different concentration of Daminozide (50mg/kg or 100mg/kg) for 15 consecutive days. ($n = 7$ per group). (a) Random core body temperature at RT ($n = 6$ per group), (b) body weight decrease % ($n = 7$ per group), (c) fasting blood glucose ($n = 7$ per group), (d) GTT ($n = 7$ per group) and (e) IIT ($n = 7$ per group) of PBS group, Daminozide 50mg/kg group and Daminozide 100mg/kg group. The following experiments were conducted to compare PBS group (CON) and Daminozide 50mg/kg group (Inhibitor). (f) Food and water intake monitoring of metabolic experiments of control and Inhibitor group mice ($n = 4$ per group).

(g) AUC of Fig. 6e ($n = 7$ per group). (h) Muscle mass of control and Inhibitor group mice ($n = 8$ per group). (i) RT-qPCR analysis of *Mb*, *Vegfa*, *Myh7* in control and Inhibitor group mice ($n = 6$ per group) (j) Serum TG and T-CHO levels in control and Inhibitor group male mice ($n = 8$ per group). (k) RT-qPCR analysis of transcribed intron fragments (peak 35364, peak 35366, peak 35370) in control and Inhibitor group mice ($n = 6$ per group). Data were expressed as mean \pm SEM. Statistical significance was assessed by one-way ANOVA (a-c), two-way ANOVA (d, e) followed with Bonferroni's multiple comparisons test or two-sided Student's *t*-test (f-k).

Reporting Summary

Nature Portfolio wishes to improve the reproducibility of the work that we publish. This form provides structure for consistency and transparency in reporting. For further information on Nature Portfolio policies, see our [Editorial Policies](#) and the [Editorial Policy Checklist](#).

Statistics

For all statistical analyses, confirm that the following items are present in the figure legend, table legend, main text, or Methods section.

n/a Confirmed

- The exact sample size (n) for each experimental group/condition, given as a discrete number and unit of measurement
- A statement on whether measurements were taken from distinct samples or whether the same sample was measured repeatedly
- The statistical test(s) used AND whether they are one- or two-sided
Only common tests should be described solely by name; describe more complex techniques in the Methods section.
- A description of all covariates tested
- A description of any assumptions or corrections, such as tests of normality and adjustment for multiple comparisons
- A full description of the statistical parameters including central tendency (e.g. means) or other basic estimates (e.g. regression coefficient) AND variation (e.g. standard deviation) or associated estimates of uncertainty (e.g. confidence intervals)
- For null hypothesis testing, the test statistic (e.g. F , t , r) with confidence intervals, effect sizes, degrees of freedom and P value noted
Give P values as exact values whenever suitable.
- For Bayesian analysis, information on the choice of priors and Markov chain Monte Carlo settings
- For hierarchical and complex designs, identification of the appropriate level for tests and full reporting of outcomes
- Estimates of effect sizes (e.g. Cohen's d , Pearson's r), indicating how they were calculated

Our web collection on [statistics for biologists](#) contains articles on many of the points above.

Software and code

Policy information about [availability of computer code](#)

Data collection

Flow cytometry data was acquired using MACSQuant (Miltenyi Biotec, Auvurn, CA, USA).
Gene expression data was collected and analyzed using Real-Time PCR System (ABI 7500). Nano-drop 2000 (Thermo Scientific, DE, USA)
Immunofluorescence images were collected using Olympus fluoview FV1000.
Leica ST5010 Autostainer XL microscope (Leica Biosystems, Wetzlar, Germany).
Metabolic studies were collected using Columbus Instruments metabolic cages (Columbus Instruments, Columbus, OH, USA).
The Electron Microscopy studies were collected using a JEOL 1200EX transmission electron microscope equipped with an AMT 2k CCD camera.
Seahorse assay was collected using a Seahorse XFe24 analyzer (Agilent Technologies, Santa Clara, CA, USA).
Bruker's Minispec Whole Body Composition Analyzer (Minispec LF 90II)
Treadmill (ZS-PT-III, Zhongshi, Beijing)
The microplate reader microcorder (Synergy 2, Bio Tek, USA)
RNA-seq data on an Illumina HISEQ 2500 and the Hisat2 v2.0.4 software (the Center for Computational Biology, Baltimore, Maryland) was used to map cleaned reads to the mm10 reference genome.
ChIP-seq: the purified DNA library was then sequenced on a Novaseq6000 sequencer (Illumina) with PE150 model by SeqHealth (Wuhan, China). The established library quantified using the Qubit 2.0, and sequenced on the Illumina HiSeq2500 PE150.

Data analysis

Data analysis was performed by GraphPad Prism 5 software.
Flow cytometry data was analyzed by FlowJo software v10.5.3.
Muscle size and Western blot data were analyzed by ImageJ software 1.53q.
The metabolic cage data analysis by the Oxymax software (Columbus Instruments, Columbus, OH, USA).

RNA-seq analysis on the Cuffnorm version 2.2.1 software.

ChIP-seq analysis :Trimmomatic (version 0.36),STAR software (version 2.5.3a), RSeQC (version 2.6),MACS2 (version 2.1.1),Homer (version v4.10),deep Tools (version 2.4.1) ,ChIP seeker (version 1.5.1), IGV (version 2.4.16),Homer (version v4.10),KOBAS software (version: 2.1.1),

For manuscripts utilizing custom algorithms or software that are central to the research but not yet described in published literature, software must be made available to editors and reviewers. We strongly encourage code deposition in a community repository (e.g. GitHub). See the Nature Portfolio [guidelines for submitting code & software](#) for further information.

Data

Policy information about [availability of data](#)

All manuscripts must include a [data availability statement](#). This statement should provide the following information, where applicable:

- Accession codes, unique identifiers, or web links for publicly available datasets
- A description of any restrictions on data availability
- For clinical datasets or third party data, please ensure that the statement adheres to our [policy](#)

The data that support the findings of this study are provided within the manuscript and Supplementary Information file. The RNA-seq data (<https://www.ncbi.nlm.nih.gov/sra/PRJNA1163094>) and ChIP-seq data (<https://www.ncbi.nlm.nih.gov/sra/PRJNA1165927>) both have been deposited in the NCBI public repository Sequence Read Archive.

Research involving human participants, their data, or biological material

Policy information about studies with [human participants or human data](#). See also policy information about [sex, gender \(identity/presentation\), and sexual orientation](#) and [race, ethnicity and racism](#).

Reporting on sex and gender	In the clinical specimens we collected, both men and women were included. We have indicated gender in supplementary materials. The study was conducted in both male and female mice
Reporting on race, ethnicity, or other socially relevant groupings	Differences between different racial, ethnic, or socially relevant groups were not explored or compared in our study. In human related research, we have complied with ethical guidelines, including obtaining the necessary ethical approvals or consents to protect the rights and interests of participants.
Population characteristics	Skeletal muscles were procured from a cohort of patients who had undergone surgical procedures for benign diseases. They were divided into three groups: BMI \leq 24; 24<BMI<28; 28 \leq BMI. Patients suffered infectious diseases, metabolic diseases (fatty liver, diabetes, thyroid disorders, hypertension, etc.), malignant tumors and pregnancy were excluded. Clinical characteristics of the participants are delineated in Table S1.
Recruitment	skeletal muscles were procured from a cohort of patients who had undergone surgical procedures for benign diseases. Patients suffered infectious diseases, metabolic diseases (fatty liver, diabetes, thyroid disorders, hypertension, etc.), malignant tumors and pregnancy were excluded. Participants were recruited in a manner devoid of self-selection and through random processes.
Ethics oversight	Human investigations were carried out in accordance with NIH guidelines and obtained approval from the Institutional Review Board (IRB) of Tongji Hospital (TJ-IRB20230926).

Note that full information on the approval of the study protocol must also be provided in the manuscript.

Field-specific reporting

Please select the one below that is the best fit for your research. If you are not sure, read the appropriate sections before making your selection.

Life sciences Behavioural & social sciences Ecological, evolutionary & environmental sciences

For a reference copy of the document with all sections, see nature.com/documents/nr-reporting-summary-flat.pdf

Life sciences study design

All studies must disclose on these points even when the disclosure is negative.

Sample size	The sample size was determined to ensure both statistical significance and result reproducibility. Based on animal welfare guidelines, the maximum number of available mice was utilized for each experiment. For in vivo experiments, cohort size was determined based on the specific experiment type and animal availability, with littermates consistently employed in each experiment. The sample size for in vivo experiments ranged from 5 to 12 mice per group. For in vitro experiments, no sample size calculation was performed. The sample size was determined to ensure both statistical significance and result reproducibility. The sample sizes of experiments were indicated in legends. For the collection of clinical samples, the sample size was determined based on the availability of clinical material.
Data exclusions	No data was excluded.
Replication	All data were derived from independently replicated experiments using distinct biological samples. These experiments were independently repeated a minimum of two times, yielding consistent results across multiple repetitions. The data were generated through independent

experiments using distinct biological samples. Each experiment was conducted independently and repeated a minimum of two times, producing consistent results.

Randomization In vitro experiments, cells were plated in to culture dishes under the same condition before treatment. The cells in different dish/well were allocated to different treatment group randomly.
Mice were randomly allocated into groups for ND feeding, HFD feeding, inhibition injection or AAV injection.
Human skeletal muscle samples: None of the patients had significant systemic disease, chronic infection, or previous history of myocardial infarction. They were grouped according to BMI.

Blinding In order to reduce subjective bias and improve the objectivity of the study, a series of measures were taken to ensure that the experimentalists did not have any information related to age, diet or treatment at the time of data collection and analysis. The analyses were conducted in a blinded manner, without consideration of the data's affiliation with any particular experimental groups. In the experiment, the data is grouped, processed and collected by a dedicated person, while the data is analyzed by someone else to avoid information leakage.

Reporting for specific materials, systems and methods

We require information from authors about some types of materials, experimental systems and methods used in many studies. Here, indicate whether each material, system or method listed is relevant to your study. If you are not sure if a list item applies to your research, read the appropriate section before selecting a response.

Materials & experimental systems

n/a	Involved in the study
<input type="checkbox"/>	<input checked="" type="checkbox"/> Antibodies
<input type="checkbox"/>	<input checked="" type="checkbox"/> Eukaryotic cell lines
<input checked="" type="checkbox"/>	<input type="checkbox"/> Palaeontology and archaeology
<input type="checkbox"/>	<input checked="" type="checkbox"/> Animals and other organisms
<input checked="" type="checkbox"/>	<input type="checkbox"/> Clinical data
<input checked="" type="checkbox"/>	<input type="checkbox"/> Dual use research of concern
<input checked="" type="checkbox"/>	<input type="checkbox"/> Plants

Methods

n/a	Involved in the study
<input type="checkbox"/>	<input checked="" type="checkbox"/> ChIP-seq
<input type="checkbox"/>	<input checked="" type="checkbox"/> Flow cytometry
<input checked="" type="checkbox"/>	<input type="checkbox"/> MRI-based neuroimaging

Antibodies

Antibodies used

The primary antibodies used are listed as follows:
Antibodies for immunoblot:
Rabbit anti-lysine-pan-monomethylation (1:1000) (CST, 14679)
Anti-lysine-pan-dimethylation (1:1000) (CST, 14117)
Anti-lysine-pan-trimethylation (1:1000) (CST, 14680)
Rabbit anti-phospho-ACCser79 (1:1000) (CST, 3661s)
Rabbit anti-ACC (1:1000) (CST, 3676s)
Rabbit anti-Cpt1a (1:1000) (Proteintech, 15184-1-AP)
Rabbit anti-PGC1 α (1:1000) (Abcam, ab54481)
Rabbit anti-Lamin B1 (1:1000) (Proteintech,12987-1-AP)
Mouse anti- β -Actin (1:1000) (Abclonal, AC026)
Rabbit anti-Flag (1:1000) (Proteintech, 20543-1-AP)
Rabbit anti-Myh7 (1:1000) (Abclonal, A22140)
Rabbit anti-Myh4 (1:1000) (Abclonal, A15293)
Rabbit anti-Mrg15(1:1000) (Abclonal, A7071)
Rabbit anti-Mrg15(1:100) (Abcam, ab183663)
Rabbit anti-Kdm2a (1:1000) (Abcam, ab191387)
Rabbit anti-H3K36me2 (1:1000) (Abcam, ab176921)
Mouse anti-Sdhb (1:1000) (Abcam, ab14714)
Rabbit anti-Ndufs1 (1:1000) (Abcam, ab169540)
Mouse anti-Ndufs3(1:1000) (Abcam, ab110246)
Rabbit anti- α -SMA(1:200) (Boster, BM3902)
HRP-conjugated Goat anti-Rabbit IgG (H+L) (1:10000) (Abclonal, AS014)
HRP-conjugated Goat anti-Mouse IgG (H+L) (1:10000) (Abclonal, AS003)
Rabbit anti-Ucp1 (1:1000) (Abcam, ab209483)
Rabbit anti-Histone 3(1:1000) (Abcam, ab1791)
Rabbit anti-H3K36me3 (1:1000) (Abcam, ab9050)
Antibodies for immunofluorescence:
Mouse anti-CD31(1:200) (CST, 3528)
Anti-mouse Alexa Fluor 488 (Jackson ImmunoResearch, 115-545-003)
Anti-rabbit Alexa Fluor 594 (Jackson ImmunoResearch, 111-585-003)
Rabbit anti-Laminin (1:1000) (Merck, L0663)
Rabbit anti-MHC I (1:200) (Merck, M8421)
Rabbit anti-MHC II(1:200) (Merck, M4276)
Rabbit anti-Esrrg(1:1000) (Abclonal, A9606; Abcam, ab219547)

All antibodies were purchased from commercial companies. The antibodies have been tested by the manufacturers.

Rabbit anti-lysine-pan-monomethylation (1:1000) (CST, 14679) can be found in 17 citations. The manufacturer provides antibody testing data: <https://www.cellsignal.cn/products/primary-antibodies/mono-methyl-lysine-mme-k-multimab-rabbit-mab-mix/14679>

Anti-lysine-pan-dimethylation (1:1000) (CST, 14117) can be found in 12 citations. The manufacturer provides antibody testing data: <https://www.cellsignal.cn/products/primary-antibodies/di-methyl-lysine-motif-dme-k-multimab-rabbit-mab-mix/14117>

Anti-lysine-pan-trimethylation (1:1000) (CST, 14680) can be found in 19 citations. The manufacturer provides antibody testing data: <https://www.cellsignal.cn/products/primary-antibodies/tri-methyl-lysine-motif-tme-k-d11x-rabbit-mab/14680>

Rabbit anti-phospho-ACCser79 (1:1000) (CST, 3661s) can be found in 1177 citations. The manufacturer provides antibody testing data: <https://www.cellsignal.cn/products/primary-antibodies/phospho-acetyl-coa-carboxylase-ser79-antibody/3661>

Rabbit anti-ACC (1:1000) (CST, 3676s) can be found in 745 citations. The manufacturer provides antibody testing data: <https://www.cellsignal.cn/products/primary-antibodies/acetyl-coa-carboxylase-c83b10-rabbit-mab/3676>

Rabbit anti-Cpt1a (1:1000) (Proteintech, 15184-1-AP) can be found in 346 citations. The manufacturer provides antibody testing data: <https://www.ptgcn.com/products/CPT1A-Antibody-15184-1-AP.htm>

Rabbit anti-PGC1 α (1:1000) (Abcam, ab54481) can be found in 548 citations. The manufacturer provides antibody testing data: <https://www.abcam.cn/products/primary-antibodies/pgc1-alpha-beta-antibody-bsa-and-azide-free-ab54481.html>

Rabbit anti-Lamin B1 (1:1000) (Proteintech, 12987-1-AP) can be found in 1116 citations. The manufacturer provides antibody testing data: <https://www.ptgcn.com/products/LMNB1-Antibody-12987-1-AP.htm>

Mouse anti- β -Actin (1:1000) (Abclonal, AC026) can be found in 2220 citations. The manufacturer provides antibody testing data: <https://abclonal.com.cn/catalog/AC026>

Rabbit anti-Flag (1:1000) (Proteintech, 20543-1-AP) can be found in 1009 citations. The manufacturer provides antibody testing data: <https://www.ptgcn.com/products/Flag-Tag-Antibody-20543-1-AP.htm>

Rabbit anti-Myh7 (1:1000) (Abclonal, A22140) has no citation yet. The manufacturer provides antibody testing data: <https://abclonal.com.cn/catalog/A22140#PublicationShow>

Rabbit anti-Myh4 (1:1000) (Abclonal, A15293) can be found in 10 citations. The manufacturer provides antibody testing data: <https://abclonal.com.cn/catalog/A15293>

Rabbit anti-Mrg15(1:1000) (Abclonal, A7071) has no citation yet. The manufacturer provides antibody testing data: <https://abclonal.com.cn/catalog/A7071#PublicationShow>

Rabbit anti-Mrg15(1:100) (Abcam, ab183663) can be found in 1 citation. The manufacturer provides antibody testing data: <https://www.abcam.cn/products/primary-antibodies/mrg15-antibody-ab183663.html>

Rabbit anti-Kdm2a (1:1000) (Abcam, ab191387) can be found in 20 citations. The manufacturer provides antibody testing data: <https://www.abcam.cn/products/primary-antibodies/kdm2a-antibody-epr18602-ab191387.html>

Rabbit anti-H3K36me2 (1:1000) (Abcam, ab176921) can be found in 12 citations. The manufacturer provides antibody testing data: <https://www.abcam.cn/products/primary-antibodies/histone-h3-di-methyl-k36-antibody-epr169942-chip-grade-ab176921.html>

Mouse anti-Sdhd (1:1000) (Abcam, ab14714) can be found in 276 citations. The manufacturer provides antibody testing data: <https://www.abcam.cn/products/primary-antibodies/sdhd-antibody-21a11ae7-ab14714.html>

Rabbit anti-Ndufs1 (1:1000) (Abcam, ab169540) can be found in 26 citations. The manufacturer provides antibody testing data: <https://www.abcam.cn/products/primary-antibodies/ndufs1-antibody-epr11521b-ab169540.html>

Mouse anti-Ndufs3(1:1000) (Abcam, ab110246) can be found in 72 citations. The manufacturer provides antibody testing data: <https://www.abcam.cn/products/primary-antibodies/ndufs3-antibody-3f9dd2-ab110246.html>

Rabbit anti- α -SMA(1:200) (Boster, BM3902) can be found in 78 citations. The manufacturer provides antibody testing data: https://www.boster.com.cn/index/products/productsDetail?goods_sn=BM3902

HRP-conjugated Goat anti-Rabbit IgG (H+L) (1:10000) (Abclonal, AS014) can be found in 1724 citations. The manufacturer provides antibody testing data: <https://abclonal.com.cn/catalog/AS014>

HRP-conjugated Goat anti-Mouse IgG (H+L) (1:10000) (Abclonal, AS003) can be found in 920 citations. The manufacturer provides antibody testing data: <https://abclonal.com.cn/catalog/AS003>

Rabbit anti-Ucp1 (1:1000) (Abcam, ab209483) can be found in 36 citations. The manufacturer provides antibody testing data: <https://www.abcam.cn/products/primary-antibodies/ucp1-antibody-epr20381-ab209483.html>

Rabbit anti-Histone 3(1:1000) (Abcam, ab1791) can be found in 4739 citations. The manufacturer provides antibody testing data: <https://www.abcam.cn/products/primary-antibodies/histone-h3-antibody-nuclear-marker-and-chip-grade-ab1791.html>

Rabbit anti-H3K36me3 (1:1000) (Abcam, ab9050) can be found in 975 citations. The manufacturer provides antibody testing data: <https://www.abcam.cn/products/primary-antibodies/histone-h3-tri-methyl-k36-antibody-chip-grade-ab9050.html>

Eukaryotic cell lines

Policy information about [cell lines and Sex and Gender in Research](#)

Cell line source(s)	C2C12 myoblasts(ATCC Cat# CRL-1772; RRID: CVCL_0188).
Authentication	Cell lines used were not authenticated.
Mycoplasma contamination	Mycoplasma contamination was not detected during cell culture.
Commonly misidentified lines (See ICLAC register)	Cell lines employed in the study were not among the list of misidentified lines.

Animals and other research organisms

Policy information about [studies involving animals](#); [ARRIVE guidelines](#) recommended for reporting animal research, and [Sex and Gender in Research](#)

Laboratory animals	The Kdm2aflox/flox (Kdm2af1/fl) mice in the C57BL/6 background were generated by targeting exons 7–9 (encoding the JmJc-catalytic domain) using a Cre-LoxP system. The Flp transgenic mice and ACTA1-rtTA, tetO-cre mice were purchased from the Jackson's Laboratory (Bar Harbor, ME, USA; Number: 012433). 8-week-old C57BL/6 (WT) mice were purchased from Beijing HFK Bioscience (Beijing, China). All mice were maintained under specific pathogenfree conditions at the Tongji Hospital Animal Center with 20–24°C ambient temperature, 45–65% humidity, and a 12/12h light/dark cycle. Both 8-week-old ACTA1-rtTA, tetO-cre-Kdm2af1/fl (referred as knockout (Kdm2aSKO)) mice and their Kdm2af1/fl littermates (referred as wild-type (Kdm2af1/fl) controls) were either maintained on normal diet or switched to high fat diet for 16 consecutive weeks. Mice were allocated to ND group or HFD group randomly.
Wild animals	The study did not involve the utilization of any wild animals.
Reporting on sex	The male and female C57BL/6 (B6) wild-type (WT) mice were used in our animal experiments, which usually have little biological variation and are relatively stable. The number of mice used in different groups in specific experiments has been indicated in the manuscript and supplemental materials.
Field-collected samples	The study did not involve samples collected from the field.
Ethics oversight	Ethical clearance for all animal procedures was granted by the Tongji Hospital Animal Care and Use Committee (Approval Code: TJH-TJH-202204022), following the guidelines outlined by the National Institutes of Health (NIH) in the United States.

Note that full information on the approval of the study protocol must also be provided in the manuscript.

Plants

Seed stocks	<i>Report on the source of all seed stocks or other plant material used. If applicable, state the seed stock centre and catalogue number. If plant specimens were collected from the field, describe the collection location, date and sampling procedures.</i>
Novel plant genotypes	<i>Describe the methods by which all novel plant genotypes were produced. This includes those generated by transgenic approaches, gene editing, chemical/radiation-based mutagenesis and hybridization. For transgenic lines, describe the transformation method, the number of independent lines analyzed and the generation upon which experiments were performed. For gene-edited lines, describe the editor used, the endogenous sequence targeted for editing, the targeting guide RNA sequence (if applicable) and how the editor was applied.</i>
Authentication	<i>Describe any authentication procedures for each seed stock used or novel genotype generated. Describe any experiments used to assess the effect of a mutation and, where applicable, how potential secondary effects (e.g. second site T-DNA insertions, mosaicism, off-target gene editing) were examined.</i>

ChIP-seq

Data deposition

- Confirm that both raw and final processed data have been deposited in a public database such as [GEO](#).
- Confirm that you have deposited or provided access to graph files (e.g. BED files) for the called peaks.

Data access links <i>May remain private before publication.</i>	The raw data have been deposited in the NCBI public repository Sequence Read Archive, with an accession number PRJNA1165927.
Files in database submission	The raw data have been deposited in the NCBI public repository Sequence Read Archive, with an accession number PRJNA1165927.
Genome browser session (e.g. UCSC)	The raw data have been deposited in the NCBI public repository Sequence Read Archive, with an accession number PRJNA1165927.

Methodology

Replicates	ChIP-seq was also conducted on the above isolated Gas tissues from three HFD Kdm2af1/fl and Kdm2aSKO mice, respectively.
Sequencing depth	Sequenced 10 G raw data on Novaseq 6000 sequencer (Illumina) with PE150 model.
Antibodies	Anti-H3K36me2(1:100)(Abcam, Cat# ab176921; RRID: AB_2941920)
Peak calling parameters	The MACS2 software ² Version 2.1.1 ² was used for peak calling. The bedtools ² Version 2.25.0 ² was used for peaks annotation and peak distribution analysis.The differentially binding peaks were identified by csaw(version 1.30.1).The Homer ² version 4.10 ² was used for

	motifs analysis.
Data quality	Raw sequencing data was first filtered by Trimmomatic (version 0.36), low-quality reads were discarded and the reads contaminated with adaptor sequences were trimmed.
Software	The clean reads were used for protein binding site analysis. They were mapped to the reference genome of mouse from NC_000066.7 version using STAR software (version 2.5.3a) with default parameters. The RSeQC ² version 2.6 ² was used for reads distribution analysis. The MACS2 software ² Version 2.1.1 ² was used for peak calling. The bedtools ² Version 2.25.0 ² was used for peaks annotation and peak distribution analysis. The differentially binding peaks were identified by a python script ² using fisher test. The Homer ² version 4.10 ² was used for motifs analysis. Gene ontology (GO) analysis and Kyoto encyclopedia of genes and genomes (KEGG) enrichment analysis for annotated genes were both implemented by KOBAS software (version: 2.1.1) with a corrected P-value cutoff of 0.05 to judge statistically significant enrichment.

Flow Cytometry

Plots

Confirm that:

- The axis labels state the marker and fluorochrome used (e.g. CD4-FITC).
- The axis scales are clearly visible. Include numbers along axes only for bottom left plot of group (a 'group' is an analysis of identical markers).
- All plots are contour plots with outliers or pseudocolor plots.
- A numerical value for number of cells or percentage (with statistics) is provided.

Methodology

Sample preparation	C2C12 myoblasts were differentiated in 24-well plates. At day 7 of differentiation, myotubes were treated with ERthermAC (Emd millipore SCT057) (250 nM) for 30 min, and cells were then washed 3 times with PBS and subjected to Flow cytometry analysis.
Instrument	MACSQuant (Miltenyi Biotec, Auvurn, CA, USA)
Software	FlowJo software v10.5.3
Cell population abundance	FSC-A and SSC-A gating are used to determine the size and shape of cells.
Gating strategy	FSC-A and SSC-A gating are commonly used to determine the size and shape of cells, thereby helping to identify and remove debris and distinguish between different cell types. Singlets were identified by using FSC-A and FSC-H gating. Fluorescence intensity was observed in BL2 channel (590nm).

- Tick this box to confirm that a figure exemplifying the gating strategy is provided in the Supplementary Information.